ÉCOLE POLYTECHNIQUE FÉDÉRALE DE LAUSANNE

MATHICSE

Mathematics Institute of Computational Science and Engineering

School of Basic Sciences - Section of Mathematics

MATHICSE Technical Report

Nr. 38 .2016

October 2016

A fast virtual surgery platform for many scenarios haemo-dynamics of patient-specific coronary artery bypass grafts

Francesco Ballarin, Elena Faggiano, Andrea Manzoni, Gianluigi Rozza,
Alfio Quarteroni, Sonia Ippolito, Carlo Antona, Roberto Scrofani

A fast virtual surgery platform for many scenarios haemodynamics of patient-specific coronary artery bypass grafts

Francesco Ballarin · Elena Faggiano · Andrea Manzoni · Gianluigi Rozza · Alfio Quarteroni · Sonia Ippolito · Carlo Antona · Roberto Scrofani

Abstract

A fast computational framework is devised to the study of several configurations of patient-specific coronary artery bypass grafts. This is especially useful to perform a sensitivity analysis of the haemodynamics for different flow conditions occurring in native coronary arteries and bypass grafts, the investigation of the progression of the coronary artery disease and the choice of the most appropriate surgical procedure. A complete pipeline, from the acquisition of patient-specific medical images to fast parametrized computational simulations, is proposed. Complex surgical configurations employed in the clinical practice, such as Y-grafts and sequential grafts, are studied. A virtual surgery platform based on model reduction of unsteady Navier Stokes equations for blood dynamics is proposed to carry out sensitivity analyses in a very rapid and reliable way. A specialized geometrical parametrization is employed to compare the effect of stenosis and anastomosis variation on the outcome of the surgery in several relevant cases.

F. Ballarin
MOX - Modeling and Scientific Computing, Dipartimento di Matematica, Politecnico di Milano, P.za Leonardo da Vinci 32, I-20133 Milano, Italy.
Current address: mathLab, Mathematics Area, SISSA, via Bonomea 265, I-34136 Trieste, Italy. E-mail: francesco.ballarin@sissa.it

E. Faggiano
MOX - Modeling and Scientific Computing, Dipartimento di Matematica, Politecnico di Milano, P.za Leonardo da Vinci 32, I-20133 Milano, Italy.
Current address: Computational Mechanics & Advanced Materials Group, Department of Civil Engineering and Architecture, University of Pavia, via Ferrata 3, I-27100 Pavia, Italy

A. Manzoni
CMCS - Modelling and Scientific Computing, Ecole Polytechnique Fédérale de Lausanne, Station 8, CH-1015 Lausanne, Switzerland

G. Rozza
mathLab, Mathematics Area, SISSA, via Bonomea 265, I-34136 Trieste, Italy

A. Quarteroni
CMCS - Modelling and Scientific Computing, Ecole Polytechnique Fédérale de Lausanne, Station 8, CH-1015 Lausanne, Switzerland

S. Ippolito
Radiology Unit, Ospedale Luigi Sacco, Via G. B. Grassi 74, I-20157 Milano, Italy

C. Antona
Cardiovascular Surgery Unit, Ospedale Luigi Sacco, Via G. B. Grassi 74, I-20157 Milano, Italy.

R. Scrofani
Cardiovascular Surgery Unit, Ospedale Luigi Sacco, Via G. B. Grassi 74, I-20157 Milano, Italy.

Nomenclature

Coronary arteries of the right coronary tree:
RCA: right coronary artery;
PDA: posterior descending artery;
PL: postero-lateral artery.
Coronary arteries of the left coronary tree:
LCA: main trunk of the left coronary artery;
LAD: left anterior descending artery;
Diag.: diagonal branch of the left anterior descending artery;
LCX: left circumflex artery;
OM: obtuse marginal artery.
Bypass grafts:
LITA: left internal thoracic artery;
Rad.: radial artery bypass grafts;
SVG: saphenous vein bypass grafts.

1 Introduction

Coronary artery bypass grafting (CABG) is a surgical procedure in which one or more grafts are used to restore blood flows to the myocardium when severe *coronary artery disease (CAD)* occurs. In this case, the occlusion of one or

several major coronary arteries undermines the perfusion of oxygen-rich blood to the heart. Although several alternative treatments exist, CABG is still one of the most widespread surgical practice worldwide (Puskas et al., 2014). However, current clinical experience suggests that, after some years, the implanted vessels themselves tend to occlude due to the process of intimal thickening (see Figure 1), leading to the failure of the surgery and ultimately to the need of reintervention (Puskas et al., 2014; Kirklin and Barratt-Boyes, 1988; Go et al., 2014).

A vast clinical experience is available on this subject since the early attempts on CABG in the 50s: it concerns preliminary assessment of the disease, choices of the bypass grafts and anastomosis locations during surgery, and survey of clinical outcomes after surgery (Kirklin and Barratt-Boyes, 1988). A better understanding of the haemodynamics in CABGs, both through experimental measurements and numerical simulations, has been achieved in the last decades, as summarized by several reviews (Ghista and Kabinejadian, 2013; Migliavacca and Dubini, 2005; Marsden, 2014; Owida et al., 2012; Taylor and Draney, 2004), dealing with either idealized (Fei et al., 1994; Inzoli et al., 1996) or patient-specific configurations (Frauenfelder et al., 2007; Dur et al., 2011; Sankaran et al., 2012). Parametric studies are of particular interest in order to assess the sensitivity of the intervention with respect to different physical conditions or surgical procedures, possibly leading to the proposal of new designs or the optimization of existing ones (Marsden, 2014).

Our aim is to apply the reduced order computational framework proposed in (Ballarin et al., 2016; Ballarin, 2015) to several three-dimensional patient-specific CABG configurations, providing a virtual platform for the sensitivity analysis of blood flows for different surgical choices under different haemodynamic conditions, properly parametrized. The three key novelties in this work are concerned with: *(i)* the use of patient-specific geometries of complete, sequential bypass grafts, *(ii)* their integration in a parametrized framework to handle physical and, in particular, geometrical variations *without* any new segmentation or remeshing, by considering a small number of clinically relevant input parameters, and *(iii)* their integration in a computational reduction framework to obtain numerical simulations for each new value of input parameters *without* querying expensive high fidelity (e.g. finite element) solvers but using a reduced order solver relying on a reduced basis method. Indeed, the solution of expensive high fidelity simulations requires order of a day even on modern high performance computing architectures, while our proposed virtual platform allows to obtain a comparable solution (in terms of accuracy) in a few minutes, provided that an extensive offline stage of computations has been carried out once and for all. The main motivation behind the use of such virtual platform is that clinical interest is related not only to the simulation on a patient-specific configuration, but also to the need of addressing the variation of flow conditions and geometries to take into account several scenarios, aiming at a possible improvement of the design of the surgical operation and deeper comprehension of resulting flow conditions. Hence, the solution of expensive high fidelity simulations for *each* new physical or geometrical configuration is usually unaffordable in terms of CPU time. This limitation can only be successfully overcome by relying on a reduced order methodology such as the one detailed in this work.

2 Materials and methods

Accurate numerical simulations of CABGs on patient-specific configurations in a wide range of scenarios are obtained in this work at greatly reduced computational costs thanks to the virtual surgery platform described in (Ballarin et al., 2016). See also Figure 2 for a graphical sketch. In this section we describe the proposed computational strategy, based on *(i)* medical imaging data, *(ii)* physical and geometrical parametrization to characterize different scenarios of interest, and *(iii)* a projection based reduced order model (ROM). We refer the reader to (Hesthaven et al., 2016; Quarteroni et al., 2016) for a detailed mathematical overview of the reduced basis method, which is the key computational tool ensuring substantial savings.

2.1 Patient-specific clinical dataset and medical imaging procedure

2.1.1 Patients recruitment and clinical data

Patients enrolled for this study have undergone CABG surgery due to critical coronary artery disease. Enrolled population features a broad variability of both disease and surgical intervention, with the aim of being representative of the most common cases. A summary of available clinical cases is provided in Figure 3 and Table 1. Internal review board approval was obtained to conduct this study.

For a better understanding of the surgery, each branch is denoted by a different color in Figure 3. The right coronary tree is denoted by blue colors, while the left coronary tree is denoted by red/yellow colors. Grafts are colored with green tonalities. Table 1 summarizes surgical choices for each patient, related in particular to grafting materials (arterial grafts such as LITA or radial arteries, or venous grafts such as SVG) and their usage either as single or sequential grafts. LITA graft is employed in all patients, being the gold standard for the revascularization of the left coronary tree, and especially the LAD branch (Puskas et al., 2014). Patients differ widely on the remaining grafts, depending on the surgical choices related to the coronary artery disease. In

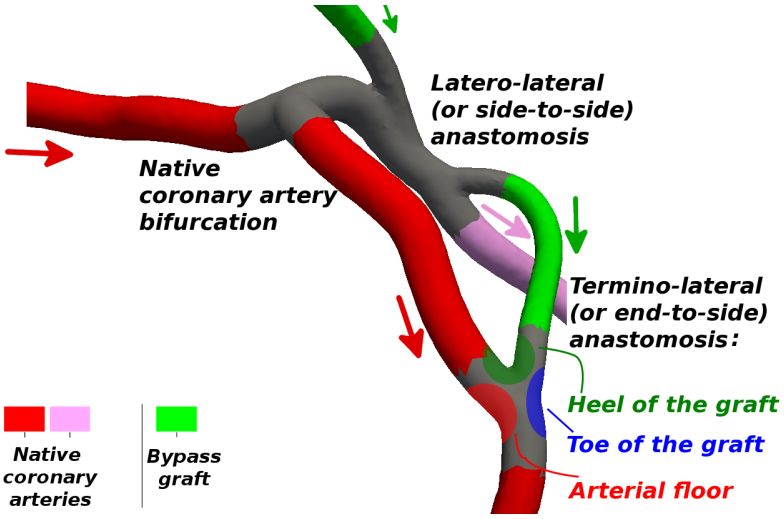

Fig. 1: Illustration of anastomosis (end-to-side and side-to-side) and bifurcations; intimal thickening of an end-to-side anastomosis typically occurs on the arterial floor and near the heel and toe of the graft. Arrows denote blood flow direction.

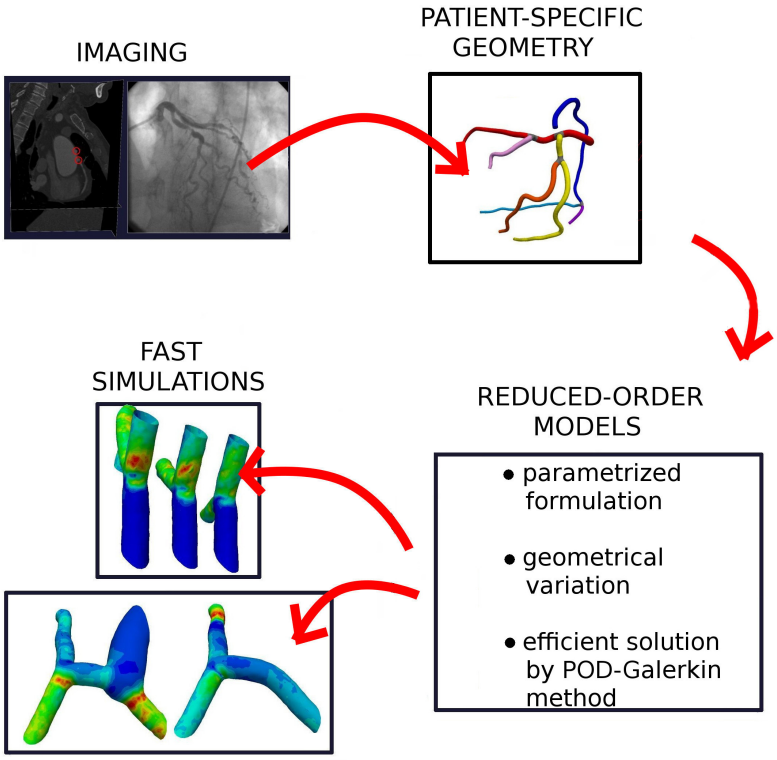

Fig. 2: A sketch of the proposed reduced order framework.

all cases but one the disease affects two, three or more vessels, hence more than one anastomosis is needed. In more then half of the patients the number of required anastomoses is larger than the available grafts, so that a sequential procedure is needed, in which a graft is used for more than one anastomosis. For each patient, the total number of bypasses is summarized in the last row of Table 1.

Available clinical data include both a pre-surgery angiographic study by means of a coronary angiography and a post-surgery computed tomography (CT) scan. A Toshiba angiography system is employed for the former, while a Philips Brilliance CT 64-slice system is employed to perform contrast enhanced CT, with a slice thickness of $0.67mm$, slice spacing of $0.4mm$, reconstruction matrix of 512×512 pixels, resolution of $0.3mm \times 0.3mm \times 0.3mm$. Acquisitions were

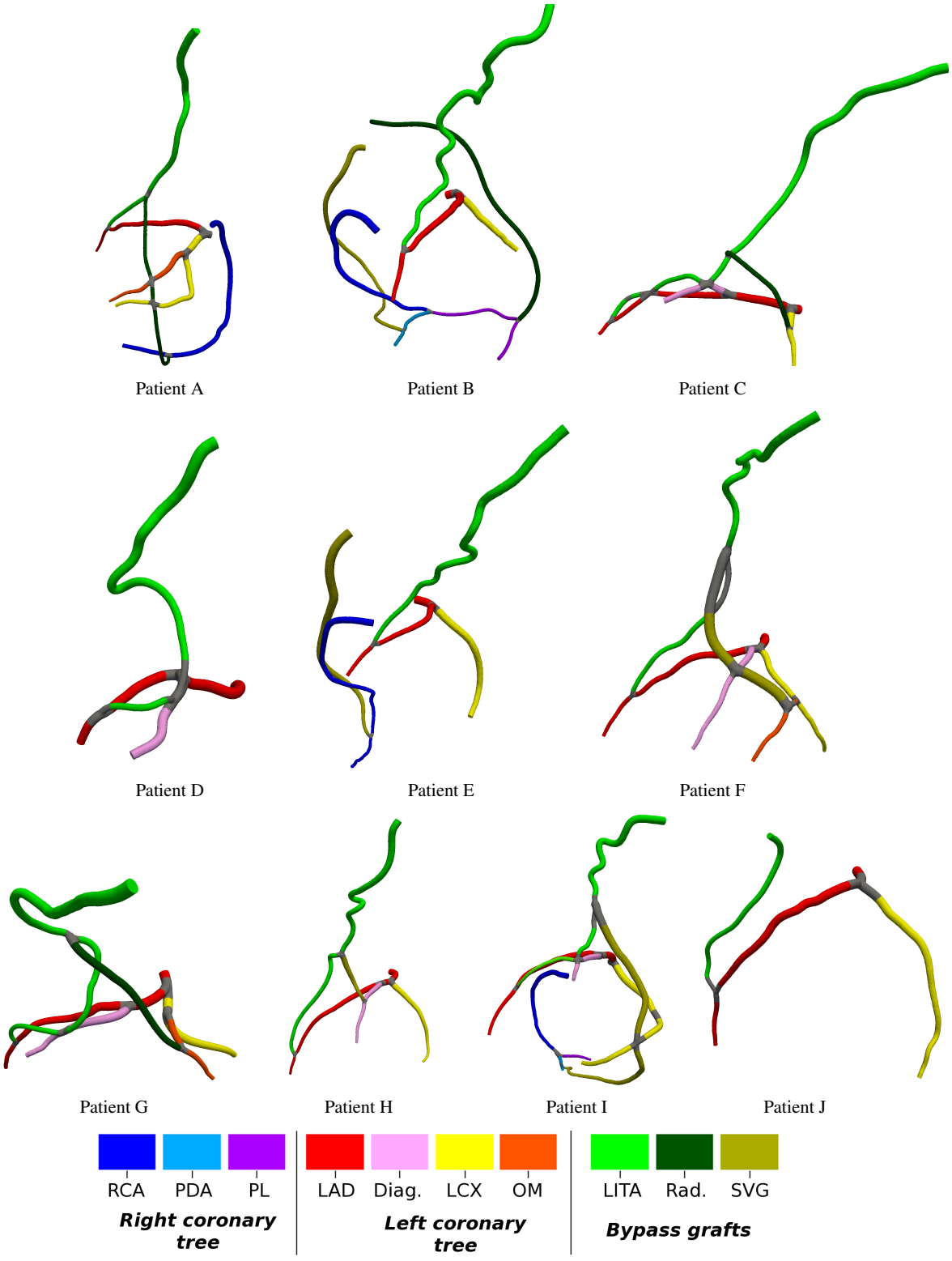

Fig. 3: Current clinical dataset.

	A	**B**	**C**	**D**	**E**	**F**	**G**	**H**	**I**	**J**
Single LITA graft	1	1			1	1		1		1
Single Rad. graft		1								
Single SVG graft		1			1					
Y-graft with LITA, single Rad. graft			1				1			
Y-graft with LITA, single SVG graft								1		
Sequential LITA grafts			3	2			2		2	
Y-graft with LITA, sequential Rad. grafts	3									
Y-graft with LITA, sequential SVG grafts						2			2	
Total number of bypass grafts	4	3	4	2	2	3	3	2	4	1

Table 1: Overview of the CABG surgery performed for each patient.

carried out at approximately the 75% of the cardiac cycle, during which the heart is in the diastolic phase. This choice is motivated by the fact that in this phase coronary arteries are less stretched and more perfused by blood.

2.1.2 Medical imaging procedure

A medical imaging pipeline has been setup to build a mesh from CT-scan clinical data, thanks to the integration with the Vascular Modelling Toolkit `vmtk` (Antiga et al., 2008). Anisotropic diffusion (Perona and Malik, 1990) and vessel enhancement filters (Frangi et al., 1998) are applied to the CT-scan image. A level set segmentation is then applied to the preprocessed image, as in (Antiga, 2002). The initialization of the level set is based on the *colliding front* method (Antiga et al., 2008). Once the level set segmentation is completed, a marching cube algorithm (Lorensen and Cline, 1987) is employed to generate a polygonal surface. However, this may yield artifacts arising either from the CT scan data or the reconstruction procedure. For these reasons, we adopt a simplifying assumption and take advantage of the fact that both coronary arteries and bypass grafts are vessels of a network of tubular structures, and use the reconstructed geometry to extract the centerlines of these tubular structures. We refer to the centerline as to the curve $\boldsymbol{\gamma}(s)$ connecting two outermost sections of the tentative geometry. The centerline $\boldsymbol{\gamma}(s)$ locally maximizes the distance from the boundary of the vessel (Antiga, 2002; Antiga et al., 2003, 2008). The value of the maximal inscribed radius $r(s)$ is also associated to each centerline point, where s denotes the curvilinear abscissa. A smoothing procedure is carried out (consisting of a running average on the coordinates, linearization of the radius with respect to the curvilinear abscissa), except near stenoses where data tabulated from angiography scan are employed to quantify the location and severity of the disease. Finally, the surface corresponding to each branch is obtained by sweeping a circular cross section of radius $r(s)$ along the centerlines $\boldsymbol{\gamma}(s)$, and the interior of the resulting network is filled with volumetric elements in order to obtain a tetrahedral volume mesh using *TetGen*. In particular, a radius adaptive mesh is generated.

2.2 Geometrical and physical parametrization

2.2.1 Geometrical parametrization for vascular vessels

In this work we consider two geometrical parameters, due to their clinical relevance for the problem at hand:

- *stenosis severity* α. This is a clinically relevant geometrical parameter; indeed, current experience suggests that surgery should be performed only for critical occlusions (Rowe et al., 1969; Hillis et al., 2011; Sabik III et al., 2005, 2003; Swillens et al., 2012). We use the virtual platform to vary stenosis factors in the range $[0, 90\%]$ in order to compare critical cases ($\alpha_j \geq 70\%$) to non-critical ones ($\alpha_j < 70\%$). The location of the stenosis and the extension of the stenosic region are kept fixed from the available clinical data. In case of double- or triple-vessel coronary artery disease, each stenosis is described by a single parameter α_j, where j denotes the stenosed artery (e.g. $j =$ LAD, LCX, RCA, etc.).
- *grafting angle* θ. Current clinical experience suggests that at least three possible termino-lateral (end-to-side) anastomoses are employed in clinical practice: antegrade (same direction for graft flow and native vessel flow in the anastomosis), T-shaped (graft perpendicular to the native vessel), and retrograde (opposite directions for graft flow and native vessel flow in the anastomosis). The virtual platform is employed to compare the haemodynamics in these different cases. The grafting angle is considered as geometrical parameter, in the range $\theta \in [25^\circ, 155^\circ]$, to deform the patient-specific configuration; antegrade cases correspond to angles close to 45°, T-shaped to 90°, and retrograde to 135°, respectively.

We exploit the *centerlines-based parametrization* proposed in (Ballarin et al., 2016) to deform the patient-specific mesh into a parametric one in an *automatic way* (i.e., without any new segmentation or remeshing, in contrast to what has been done e.g. in (Sankaran et al., 2012)). This assumption is a necessary prerequisite for the efficient application of the reduced order model, that needs to combine solutions

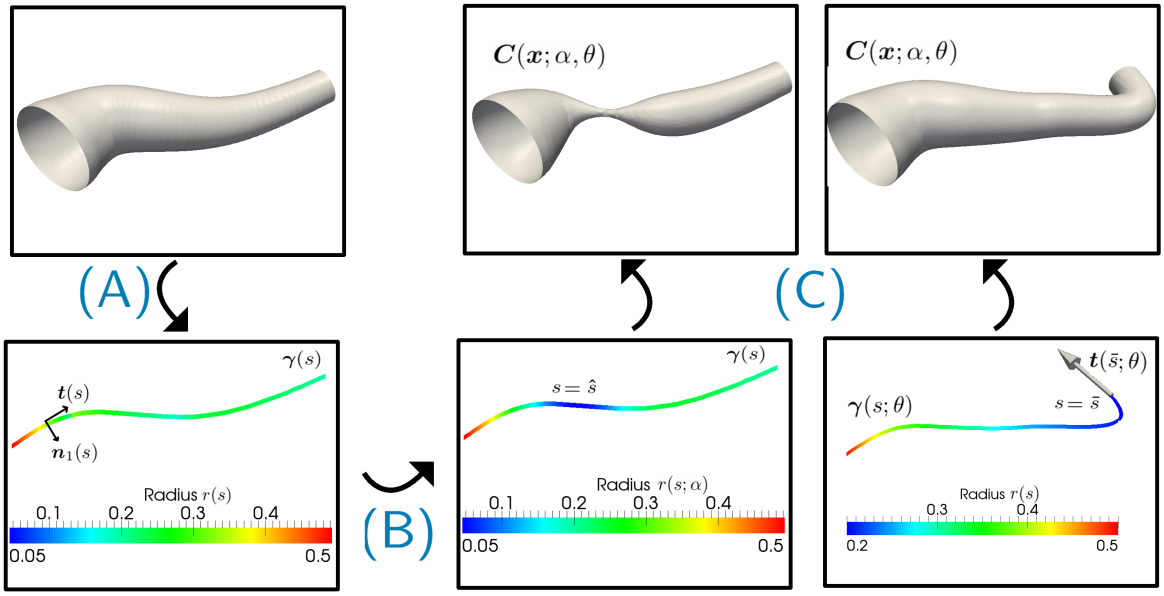

Fig. 4: A centerline based parametrization (single curve).

representing different *geometrical configurations* still represented on the *same mesh*.

More in detail, the deformation of a single branch is carried out in three steps (see Figure 4):

(A) *Preprocessing*: let $\gamma(s)$ be the centerline of the vessel, and $r(s)$ the radius of its maximum inscribed sphere. A moving coordinate frame $(\boldsymbol{t}(s), \boldsymbol{n}_1(s), \boldsymbol{n}_2(s))$ attached to $\gamma(s)$ is computed by means of a parallel transport procedure (Bishop, 1975). Three-dimensional vessels can then be represented using curvilinear cylindrical coordinates (ρ, φ, s), corresponding to the local radius, angular coordinate and curvilinear abscissa, respectively.

(B) *Curve deformation* and *radius variation*: let $\alpha \in [0, 0.9]$ be the severity of the stenosis and θ be the grafting angle. The reference radius $r(s)$ is locally decreased near the stenosis (located at $s = \hat{s}$) to obtain a parametrized radius $r(s;\alpha)$. We rotate the tangent vector $t(\bar{s})$ at the anastomosis (located at $s = \bar{s}$) of an angle θ, and apply a deformation to the reference curve $\gamma(s)$ to get a parametrized curve $\gamma(s;\theta)$.

(C) *Vessel deformation*: we exploit the cylindrical vessel representation to obtain the deformed configuration of the branch, by computing the map $\boldsymbol{C}(\cdot;\alpha,\theta) : \mathbb{R}^3 \to \mathbb{R}^3$,

$$\begin{aligned}\boldsymbol{C}(\boldsymbol{x};\alpha,\theta) =& \gamma(s(\boldsymbol{x});\theta) + \\ & \rho r(s(\boldsymbol{x});\alpha)\ [\cos\varphi(\boldsymbol{x})\ \boldsymbol{n}_1(s(\boldsymbol{x});\theta) + \\ & \sin\varphi(\boldsymbol{x})\ \boldsymbol{n}_2(s(\boldsymbol{x});\theta)]\,.\end{aligned}$$

The resulting map $\boldsymbol{C}(\cdot;\alpha,\theta)$ allows to deform the three-dimensional vessel between the patient-specific branch (as reference configuration) and a deformed configuration, obtained as a function of the stenosis α and grafting angle θ (see the right blocks of Figure 4).

These steps can be performed for each branch independently and then combined together to deform a network, as shown in Figure 5 in the case of an anastomosis. Steps (A), (B) and (C) are performed to parametrize each vessel; then, an additional step (D) is carried out on each anastomosis to impose suitable interface conditions between adjacent branches, ensuring the overall regularity of the deformation of the global geometry. Also this step is fully automatic, as shown in (Ballarin et al., 2016).

2.2.2 Physical parametrization of flow rates

In addition to the geometrical parametrization discussed so far, we also consider a physical parametrization on flow rates at each inlet of the computational model (right coronary artery, left coronary artery, internal thoracic artery), because of its clinical relevance e.g. when interested in the evaluation of the surgery under both rest or stress conditions. The parametrized flow rate is expressed as

$$q_i(t;f^i) = f^i\ \bar{q}_i(t), \quad i = \text{LCA, RCA, LITA.}$$

The parameter $f^i \in [2/3, 4/3]$ is a multiplicative factor on a reference flow rate $\bar{q}_i(t)$, adapted from (Keegan et al., 2004) (LCA and RCA) and (Ishida et al., 2001) (LITA). A plot is provided in Figure 6 for the reference cases $f^i = 1$, corresponding to time-averaged Reynolds number equal to 100 (LCA and RCA) and 130 (LITA). Note that LCA features dominant diastolic flow (i.e. coronary blood flow peaks in diastole), RCA is neither diastolic nor systolic dominant, while LITA is supposed to be systolic dominant.

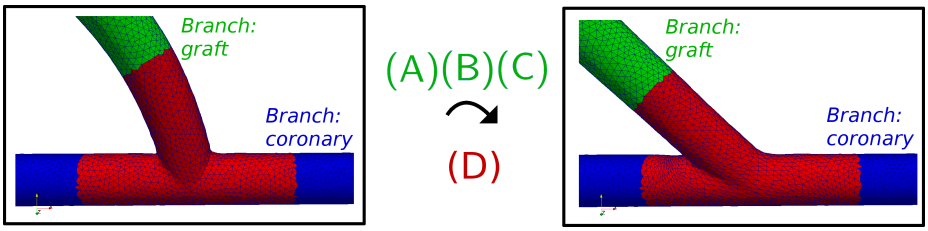

Fig. 5: A centerline based parametrization (anastomosis). Step (A), (B) and (C) are performed to deform the green branch, and step (D) is performed for the anastomosis.

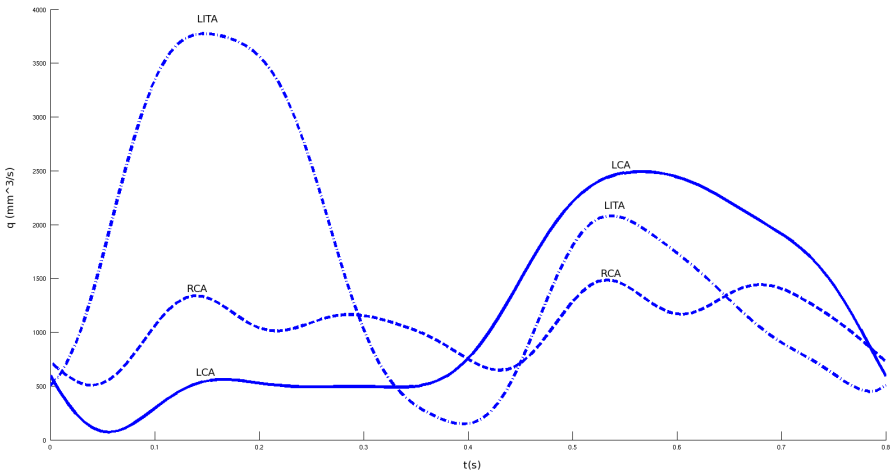

Fig. 6: Inlet flow rates q_i (LCA and RCA (Keegan et al., 2004), LITA (Ishida et al., 2001)).

2.3 POD–Galerkin reduced order models for parametrized blood flows

In this section we summarize the ROM employed in our numerical simulations. The haemodynamics in the CABG configuration is supposed to be modelled by unsteady parametrized Navier-Stokes equations, under rigid walls assumptions and constant viscosity ν: find velocity $\boldsymbol{u}$ and pressure p such that

$$\begin{cases} \frac{\partial}{\partial t}\boldsymbol{u} - \nu\Delta\boldsymbol{u} + (\boldsymbol{u}\cdot\nabla)\boldsymbol{u} + \nabla p = \mathbf{o} & \text{in } \Omega_o(\boldsymbol{\mu}_g)\times(0,T), \\ \operatorname{div}\boldsymbol{u} = 0 & \text{in } \Omega_o(\boldsymbol{\mu}_g)\times(0,T), \\ \boldsymbol{u} = \boldsymbol{g}_D(\boldsymbol{\mu}_p) & \text{on } \Gamma_D\times(0,T), \\ \boldsymbol{u} = \mathbf{o}, & \text{on } \Gamma_{o,W}(\boldsymbol{\mu}_g)\times(0,T), \\ \nu\dfrac{\partial \boldsymbol{u}}{\partial \boldsymbol{n}} - p\boldsymbol{n} = \mathbf{o}, & \text{on } \Gamma_N\times(0,T), \\ \boldsymbol{u}|_{t=0} = \boldsymbol{g}_0(\boldsymbol{\mu}_p), & \text{in } \Omega_o(\boldsymbol{\mu}_g). \end{cases}$$

The parameters are denoted by $\boldsymbol{\mu} = (\boldsymbol{\mu}_p, \boldsymbol{\mu}_g) \in \mathscr{D} \subset \mathbb{R}^{P+G}$, including both physical parametrization on the boundary conditions $\boldsymbol{\mu}_p = (f^{\text{LCA}}, f^{\text{RCA}}, f^{\text{LITA}})$ and geometrical parameters $\boldsymbol{\mu}_g = (\alpha, \theta)$, introduced in Sections 2.2.2 and 2.2.1, respectively. Thanks to the parametrization of the domain, the patient-specific configuration Ω is mapped into a parametrized one $\Omega_o(\boldsymbol{\mu}_g)$, along with it lateral boundary $\Gamma_{o,W}(\boldsymbol{\mu}_g)$. Inlet sections Γ_D and outlet sections Γ_N are fixed, and the initial condition $\boldsymbol{g}_0$ is the solution of the corresponding steady-state problem.

A FE approximation for spatial discretization and an implicit Euler scheme for time discretization are chosen as the high fidelity method, over which our proposed reduced order model is built. Let us denote by $\boldsymbol{V}_h$ and Q_h two finite-dimensional spaces for velocity and pressure, of dimension $N^h_{\mathbf{u}}$ and N^h_p, respectively, based on a FE discretization of the patient-specific geometry of mesh size h. The nonlinear system resulting from a FE discretization in space and implicit Euler discretization in time of the Navier-Stokes equations is: given $\boldsymbol{\mu} \in \mathscr{D}$ and $(\underline{\mathbf{u}}(t^n), \underline{\mathbf{p}}(t^n))$, find $(\underline{\mathbf{u}}(t^{n+1}), \underline{\mathbf{p}}(t^{n+1}))$ such that

$$\begin{bmatrix} \frac{M(\boldsymbol{\mu})}{\Delta t} + \nu A(\boldsymbol{\mu}) + C(\underline{\mathbf{u}}(t^{n+1};\boldsymbol{\mu});\boldsymbol{\mu}) & B^T(\boldsymbol{\mu}) \\ B(t^{n+1};\boldsymbol{\mu}) & 0 \end{bmatrix} \begin{bmatrix} \underline{\mathbf{u}}(t^{n+1};\boldsymbol{\mu}) \\ \underline{\mathbf{p}}(t^{n+1};\boldsymbol{\mu}) \end{bmatrix} = \begin{bmatrix} \frac{M(\boldsymbol{\mu})}{\Delta t}\underline{\mathbf{u}}(t^n;\boldsymbol{\mu}) + \underline{\mathbf{f}}(t^{n+1}) \\ \underline{\mathbf{0}} \end{bmatrix} \tag{1}$$

for each time-step $n = 0, \ldots, T/\Delta t - 1$, where $\underline{\mathbf{u}}(0)$ is the discrete counterpart of the initial condition, and the right-hand side term $\underline{\mathbf{f}}(t)$ encodes non-homogeneous Dirichlet boundary conditions through a lifting function. The parametrized tensors M, A, B and C are respectively the mass, stiffness, incompressibility and advection terms of the parametrized Navier-Stokes equations.

The proposed reduced order model is able to provide large computational speedups thanks to the separation between an offline stage (computationally expensive, but done only once) and an online stage (computationally inexpensive, carried out for each virtual scenario of interest). During the offline stage a set $\Xi_{\text{train}} = \{\boldsymbol{\mu}^1, \dots, \boldsymbol{\mu}^{N_{\text{train}}}\} \subset \mathscr{D}$ of N_{train} points, chosen randomly over the parameter space $\mathscr{D}$, is defined. For each $\boldsymbol{\mu} \in \Xi_{\text{train}}$ problem (1) is solved for $n = 0, ..., T/\Delta t - 1$, and all the corresponding solutions (both velocity and pressure) are saved. A Proper Orthogonal Decomposition (POD) (Berkooz et al., 1993; Ravindran, 2000) is performed to select the *few most relevant* velocity (pressure, respectively) basis functions, stored in matrices $Z_{\mathbf{u}}$ (Z_p, resp.) and which span the reduced basis spaces $\boldsymbol{V}_N$ and Q_N of (small) dimension $N_{\mathbf{u}}$ and N_p,. Therefore, in the online stage, a Galerkin projection on $(\boldsymbol{V}_N, Q_N)$ is carried out, and the resulting problems reads: for any $\boldsymbol{\mu} \in \mathscr{D}$, given $\underline{\mathbf{u}}_N(t^n;\boldsymbol{\mu})$, solve

$$\begin{bmatrix} \frac{M_N(\boldsymbol{\mu})}{\Delta t} + \nu A_N(\boldsymbol{\mu}) + C_N(\underline{\mathbf{u}}_N(t^{n+1};\boldsymbol{\mu});\boldsymbol{\mu}) & B_N^T(\boldsymbol{\mu}) \\ B_N(\boldsymbol{\mu}) & 0 \end{bmatrix} \begin{bmatrix} \underline{\mathbf{u}}_N(t^{n+1};\boldsymbol{\mu}) \\ \underline{\mathbf{p}}_N(t^{n+1};\boldsymbol{\mu}) \end{bmatrix} = \begin{bmatrix} \frac{M_N(\boldsymbol{\mu})}{\Delta t} \underline{\mathbf{u}}_N(t^n;\boldsymbol{\mu}) + \underline{\mathbf{f}}_N(t^{n+1}) \\ \underline{\mathbf{0}} \end{bmatrix},$$

for any $n = 0, \dots, T/\Delta t - 1$, where e.g. $A_N(\boldsymbol{\mu}) = Z_{\mathbf{u}}^T A(\boldsymbol{\mu}) Z_{\mathbf{u}}$ is now a matrix of dimension $N_{\mathbf{u}} \ll N_{\mathbf{u}}^h$. We refer to (Ballarin et al., 2016, 2015) for additional details on the analysis of this reduced order model such as the comparison between high fidelity and reduced order solutions, as well as Manzoni (2014); Rozza et al. (2013); Burkardt et al. (2006) for related reduction methods.

3 Numerical results

For each patient in the dataset we report in Table 2 the number of considered physical and geometrical parameters, discretization of the high fidelity FE approximation, and CPU times of both high fidelity and reduced order problems. A Taylor-Hood $\mathbb{P}_2 - \mathbb{P}_1$ discretization is employed for the high fidelity FE discretization; 80 steps per cardiac cycle, for 2 cardiac cycles, are simulated. We will further discuss the performance of the proposed reduced order framework in the next section.

Relevant computational indices are obtained in a post-processing stage after the reduced order simulation in order to compare the flow patterns for different values of the parameters. In particular, we analyze wall shear stress (WSS), oscillatory shear index (OSI), transversal velocity profiles, and pressure drops, because of their relation to the process of intimal thickening (Loth et al., 2008):

- the existence of a safe bandwidth of wall shear stress (defined as $\boldsymbol{t} - \boldsymbol{t} \cdot \boldsymbol{n}\ \boldsymbol{n}$, being $\boldsymbol{t}$ the traction acting on the lateral wall of outer normal $\boldsymbol{n}$) has been suggested in (Kleinstreuer et al., 1991), highlighting that both low and high WSS may favor the restenosis process. In fact, high WSS may lead to endothelial injury and cause the development of a lesion. Instead, low WSS and long particle residence time in flow recirculation zones favors the deposit of fatty materials and cholesterol on the surface of the lumen, causing the growth of the atheroma. Results are presented either as instantaneous WSS values (usually at systole or diastole) or time-averaged WSS, denoted by TAWSS, obtained as the average of WSS over a cardiac cycle $(0, T)$

$$TAWSS = \frac{1}{T} \int_0^T |\boldsymbol{WSS}(t)|\, dt;$$

- a correlation between plaque location and oscillating shear stress has been described in (Ku et al., 1985), showing that oscillations in the direction of wall shear may cause atherogenesis. To assess the oscillatory nature of WSS we employ the OSI, defined as

$$OSI = \frac{1}{2}\left[1 - \frac{\left|\int_0^T \boldsymbol{WSS}(t) dt\right|}{\int_0^T |\boldsymbol{WSS}(t)|\, dt}\right] \qquad 0 \le OSI \le 0.5;$$

- the formation of Dean vortices in the region distal to the anastomosis is detected thanks to transversal velocity profiles. In fact, secondary flow structures (i.e. perpendicular to the flow direction) are usually not negligible at the anastomosis, and the formation of a pair of vortical structures has been observed (Sherwin and Doorly, 2003).

Regions of interest are the *heel* and *toe* of the graft, and the proximal and distal *arterial floor* near the anastomosis (see also Figure 1) (Staalsen et al., 1995; Loth et al., 2008). We refer to heel of the graft as the location of the proximal suture line, while the toe of the graft refers to the distal suture line. The adjectives *proximal* and *distal* are defined with respect to the direction of the flow in the native coronary artery.

We report these computational indices for different values of the parameters on several cases of the available patient-specific dataset. To provide an easier comparison, only one or two parameters are varied at a time in the graphical visualization; the remaining parameters are set to a standard default value, chosen equal to one for flow rates factors (standard flow rate), critical values of stenosis (90%), undeformed anastomosis configuration (no variation of the grafting angle with respect to the patient-specific one). However, the reduced order methodology is capable of varying more the one parameter at a time.

We collect the results as follows, in order to discuss each scenario separately in the next section:

Patient	A	B	C	D	E
Num. physical parameters	3	0	2	2	0
LCA inlet flow rate parameters	1	no	1	1	no
RCA inlet flow rate parameters	1	no	no	no	no
LITA inlet flow rate parameters	1	no	1	1	no
Num. geometrical parameters	3	3	2	2	3
LCA parametrized stenosis	no	no	no	no	no
LAD/Diag parametrized stenosis	1	1	2	2	1
LCX/OM parametrized stenosis	1	no	no	no	no
RCA parametrized stenosis	1	1	no	no	1
Parametrized anastomosis	no	1	no	no	1
Total number of FE dofs	1 325 530	1 826 495	813 197	1 325 044	2 038 891
FE CPU time/cardiac cycle	400 $\sim$ 450 h	450 $\sim$ 500 h	200 $\sim$ 250 h	400 $\sim$ 450 h	500 $\sim$ 550 h
ROM CPU time/cardiac cycle	5 $\sim$ 15 min	25 $\sim$ 35 min	5 $\sim$ 15 min	5 $\sim$ 15 min	25 $\sim$ 35 min

Patient	F	G	H	I	J
Num. physical parameters	2	2	2	3	0
LCA inlet flow rate parameters	1	1	1	1	no
RCA inlet flow rate parameters	no	no	no	1	no
LITA inlet flow rate parameters	1	1	1	1	no
Num. geometrical parameters	3	0	2	4	2
LCA parametrized stenosis	1	no	no	no	no
LAD/Diag parametrized stenosis	1	no	2	2	1
LCX/OM parametrized stenosis	1	no	no	1	no
RCA parametrized stenosis	no	no	no	1	no
Parametrized anastomosis	no	no	no	no	1
Total number of FE dofs	970 618	1 261 527	1 624 370	1 426 060	1 219 918
FE CPU time/cardiac cycle	350 $\sim$ 400 h	350 $\sim$ 400 h	400 $\sim$ 450 h	350 $\sim$ 400 h	400 $\sim$ 450 h
ROM CPU time/cardiac cycle	5 $\sim$ 15 min	5 $\sim$ 15 min	5 $\sim$ 15 min	5 $\sim$ 15 min	25 $\sim$ 35 min

Table 2: Details of the reduced order model. FE computations are carried out on 32 processors on modern HPC clusters, and the reported CPU time is the product of the wall time and the number of processors. ROM computations are performed, instead, in serial.

I. *virtual scenario I* concerns the effect of flow rate variation in Y-grafts. Several Y-graft configurations are compared through the computation of TAWSS near the Y-graft. Both Y-graft between LITA and radial artery (Figure 7) and Y-graft between LITA and SVG (Figure 8) are considered. Two different inflow boundary conditions are studied, corresponding to standard graft flow rate ($f^{LITA} = 1$) and increased graft flow rate ($f^{LITA} = 1.33$).
II. *virtual scenario II* focuses on the effect of flow rate variation in sequential grafts. Several sequential grafts are compared through the computation of the TAWSS near the side-to-side anastomosis. A cross anastomosis of a graft employed distally for the revascularization of the right coronary tree is considered in Patient A of Figure 9, while antegrade anastomoses for the revascularization of the left coronary tree are considered in Patients C and and G of Figure 9. Also in this case, different boundary conditions are studied, corresponding to standard graft flow rate ($f^{LITA} = 1$) or increased graft flow rate ($f^{LITA} = 1.33$).
III. *virtual scenario III* is about the effect of flow rate and stenosis variation on anastomosis. As a first case, we compare surgery outcomes for different stenosis severity on the left coronary tree, by means of OSI and WSS (Figures 10 and 11). This pathology is usually surgically treated by LITA grafts. As a second case, we compare computational indices for different stenosis severity on the right coronary tree, considering in particular a case where a radial graft is employed (Figure 12)
IV. *virtual scenario IV* concerns anastomosis geometrical variation. Also in this scenario we consider both left and right coronary trees, and different grafting types. Figures 13-15 show the results on WSS, transversal velocity profiles and pressure drop for a LITA-LAD anastomosis (arterial graft) in the left coronary tree. Figure 16 details instead the numerical results on WSS on a SVG-PDA anastomosis (venous graft) in the right coronary tree.
V. finally, *virtual scenario V* studies the effect of flow rate and stenosis variation on native coronary bifurcations, especially on the left coronary tree. Results on TAWSS are provided in Figures 17-19 for three different patients. Moreover, thanks to our virtual framework it is possible to virtually remove the bypass graft and compare the haemodynamics before and after the surgery. A proof of concept of this scenario is provided in Figure 20.

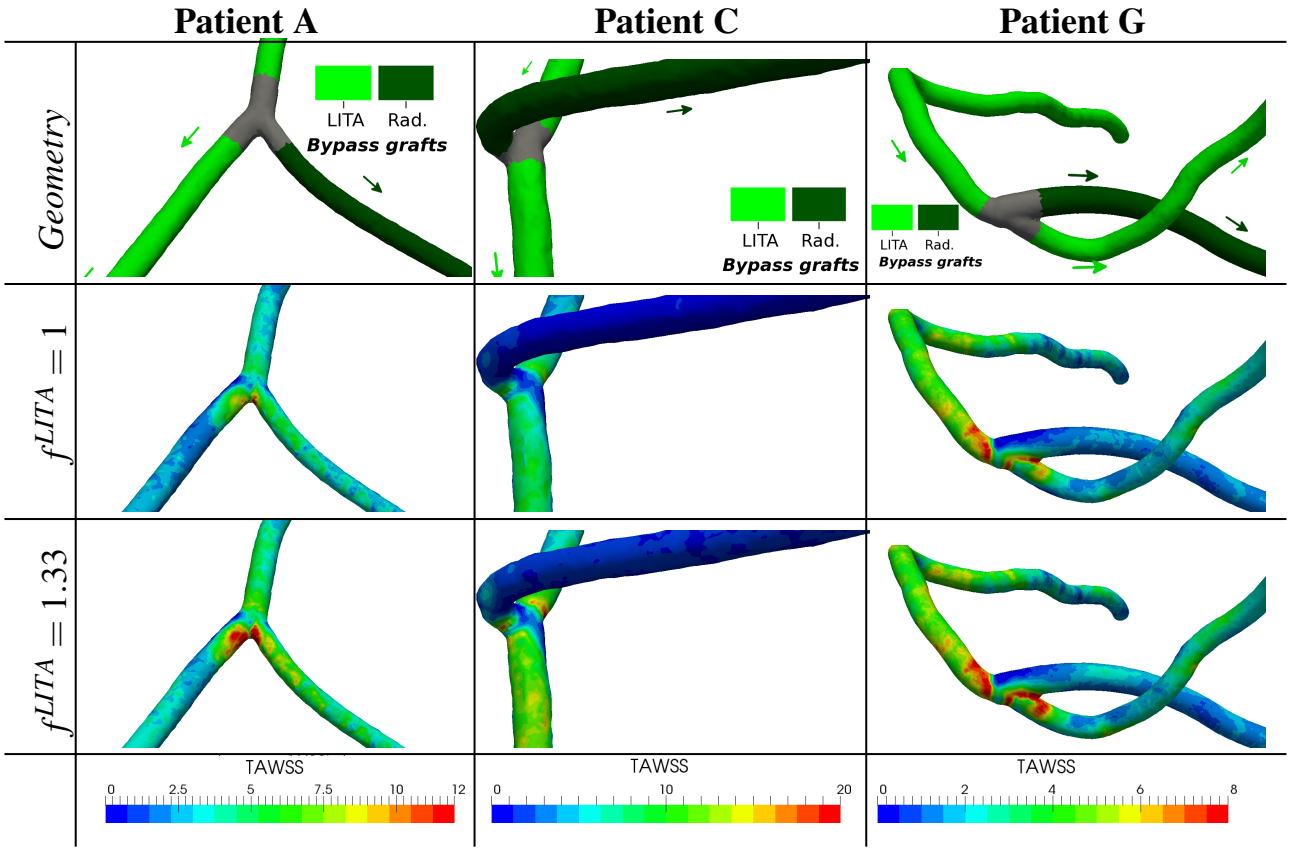

Fig. 7: *Virtual scenario I*, Y-graft between LITA and radial artery: comparison of TAWSS [Pa] for different inflow boundary conditions.

4 Discussion

4.1 State of the art on parametrized problems and novelties of the proposed virtual surgery platform

Early numerical results on three-dimensional idealized end-to-side anastomoses have been proposed in (Fei et al., 1994; Inzoli et al., 1996; Kute and Vorp, 2001; Sherwin et al., 1999), under the assumption of steady flow conditions, and in (Bertolotti and Deplano, 2000; Bertolotti et al., 2001; Deplano et al., 2001; Lei et al., 2000; Ross Ethier et al., 1998) for time-dependent flow profiles. Since these early attempts, *parametric studies* have attracted considerable attention (Pagni et al., 1997; Sabik III and Blackstone, 2008; Sabik III et al., 2003; Nordgaard et al., 2010; Swillens et al., 2012; Kute and Vorp, 2001; Keynton et al., 1991). Among these, variation of *inlet boundary conditions* is a first topic of interest, to take into account different exercise conditions of the patient (e.g. stress conditions vs rest conditions) and since variation of graft flow rate is also observed in the clinical practice in the internal thoracic artery (Pagni et al., 1997; Sabik III and Blackstone, 2008; Sabik III et al., 2003). Numerical simulations to take this aspect into account have been performed on idealized configurations (Kute and Vorp, 2001; Keynton et al., 1991), and in (Nordgaard et al., 2010; Swillens et al., 2012) on a porcine model. A parametrization of inlet boundary conditions is applied also in our work and integrated into a model reduction framework by means of multiplicative factors on inlet flow rates.

Large attention has also been paid to *local geometrical variations of CABGs* (Lei et al., 1997; Dur et al., 2011; Marsden et al., 2008; Probst et al., 2010; Sankaran and Marsden, 2010; Politis et al., 2008; Kabinejadian and Ghista, 2012; Kabinejadian et al., 2010; Wen et al., 2011), in order to propose new design or optimize existing ones performing variation of grafting angles (Fei et al., 1994; Sherwin and Doorly, 2003; Giordana et al., 2005; Keynton et al., 1991; Staalsen et al., 1995; Jackson et al., 2001; Freshwater et al., 2006; Do et al., 2011) or graft-to-host diameter ratio (Bonert et al., 2002; Qiao and Liu, 2006; Idu et al., 1999; Towne et al., 1991; Xiong and Chong, 2008). The proposed virtual surgery platform can address grafting angles variations in an automatic way (without remeshing). To the best of our knowledge this is the first study for which such an automatic procedure is applied to CABGs. Diameter ratio variation is not taken into account by the current framework. The moti-

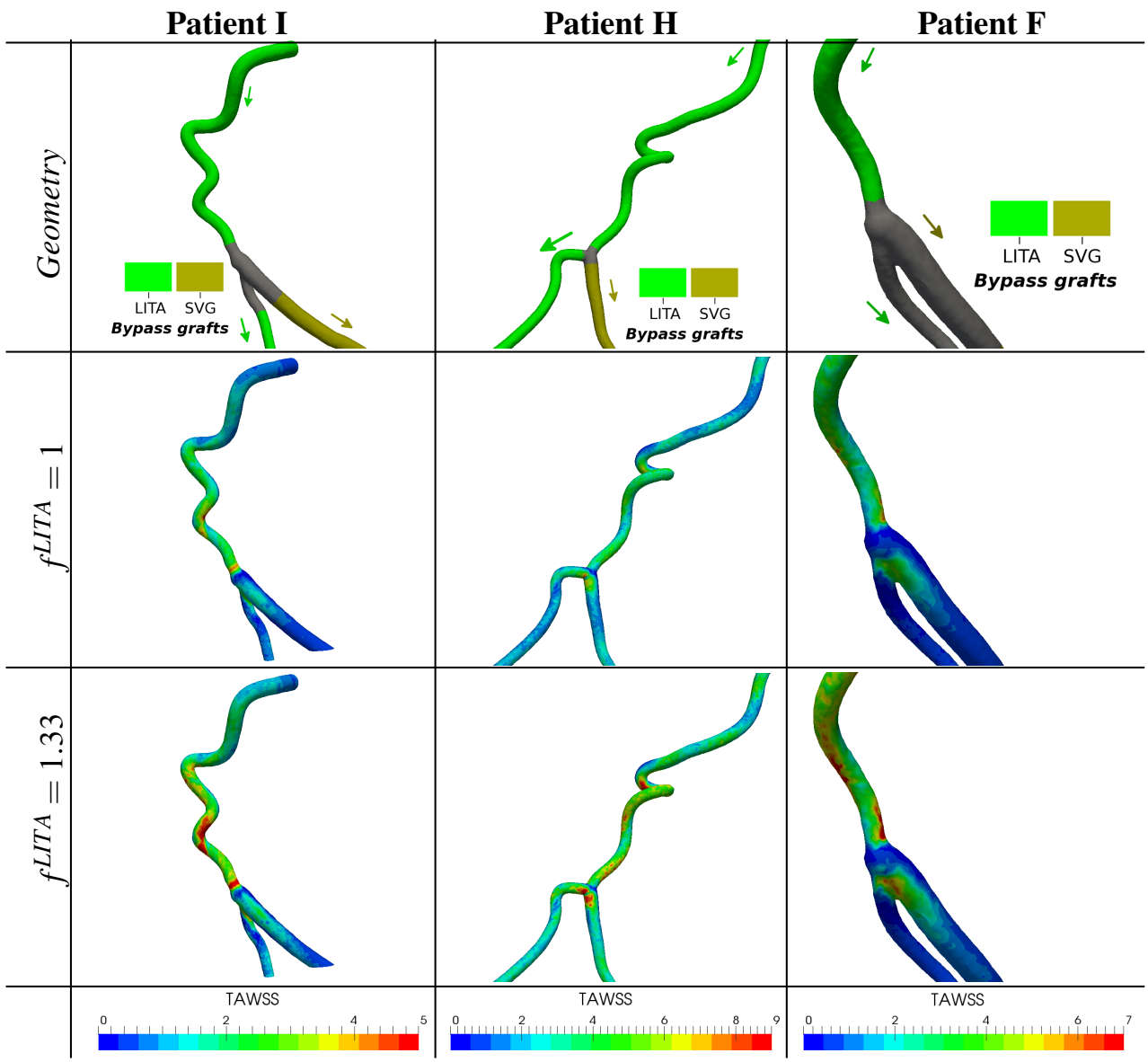

Fig. 8: *Virtual scenario I*, Y-graft between LITA and SVG: comparison of TAWSS [Pa] for different inflow boundary conditions.

vation is that grafts employed in the clinical practice come from autologous materials and thus their diameter cannot be easily varied in the clinical practice, especially considering several practical constraints in case of extensive coronary artery disease. It is thus far more important to consider a complete patient-specific network and optimize it, rather than optimize representative but idealized configurations.

Therefore, another significant feature of the present approach is the capability to carry out parametric studies on *patient-specific* CABGs. Few studies have been carried out on patient-specific configurations, reconstructed from clinical data. Among them we mention (Boutsianis et al., 2004; Chaichana et al., 2011; Kim et al., 2010) on native (healthy) coronary arteries, and (Frauenfelder et al., 2007; Dur et al., 2011; Sankaran et al., 2012; Guerciotti et al., 2016) on coronary artery bypass grafts. Our current dataset is however larger, and more complete (with respect to anastomosis features, grafting procedures, coronary artery disease) than those in previous references. In particular, (Frauenfelder et al., 2007) proposed CFD simulations only on two patients, the first one featuring a single graft and the second one a double sequential grafts. Both surgeries, however, were performed only with saphenous vein grafts, and more complex structures (such as Y-grafts) were not studied. Geometrical variations were considered instead in (Dur et al., 2011), but they were performed on two-dimensional configurations and then ap-

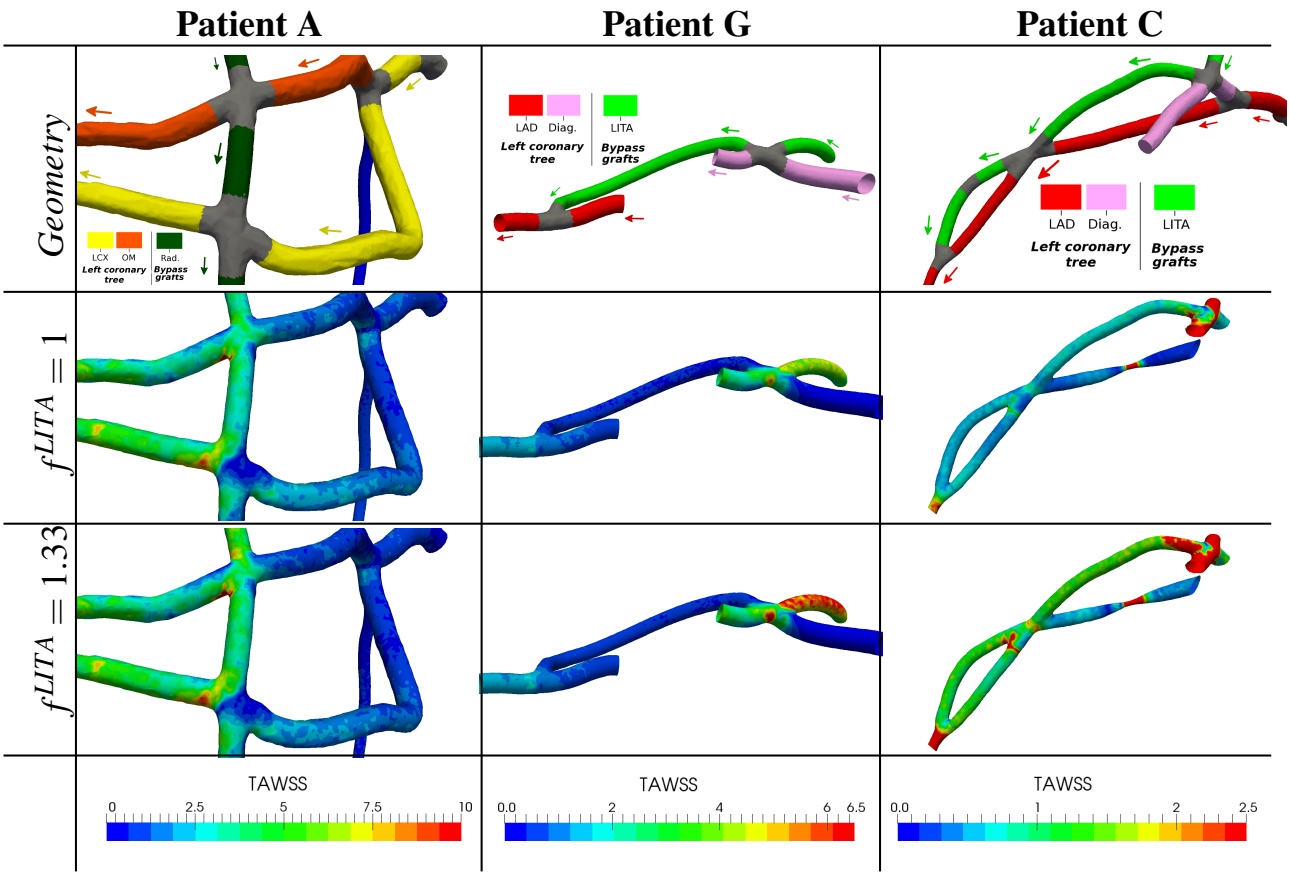

Fig. 9: *Virtual scenario II*, sequential grafts: comparison of TAWSS [Pa] for different inflow boundary conditions and stenosis.

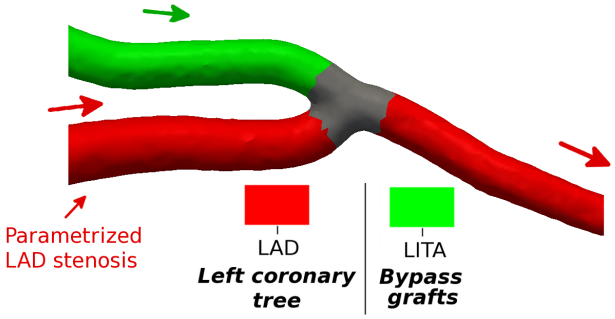

(a) Coronary arteries and bypass grafts near the studied anastomosis. Colored arrows denote blood flow direction.

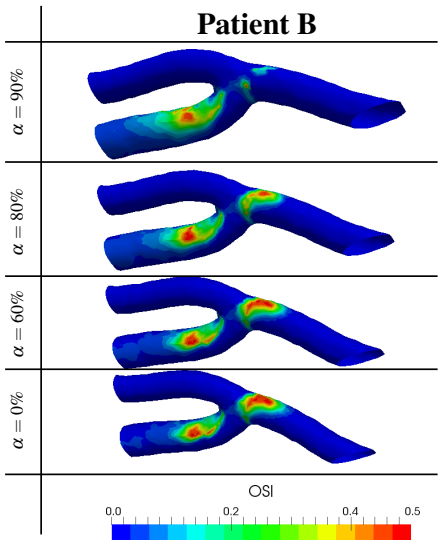

(b) OSI

Fig. 10: *Virtual scenario III*, LITA to LAD anastomosis: comparison of OSI for decreasing proximal stenosis.

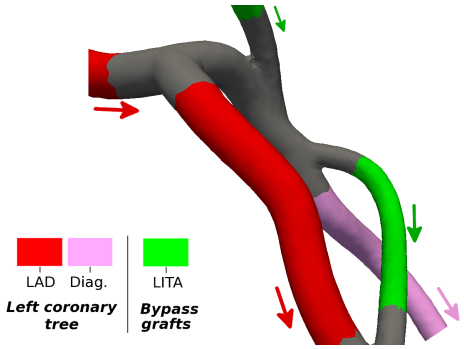

(a) Coronary arteries and bypass grafts near the studied anastomosis. Colored arrows denote blood flow direction.

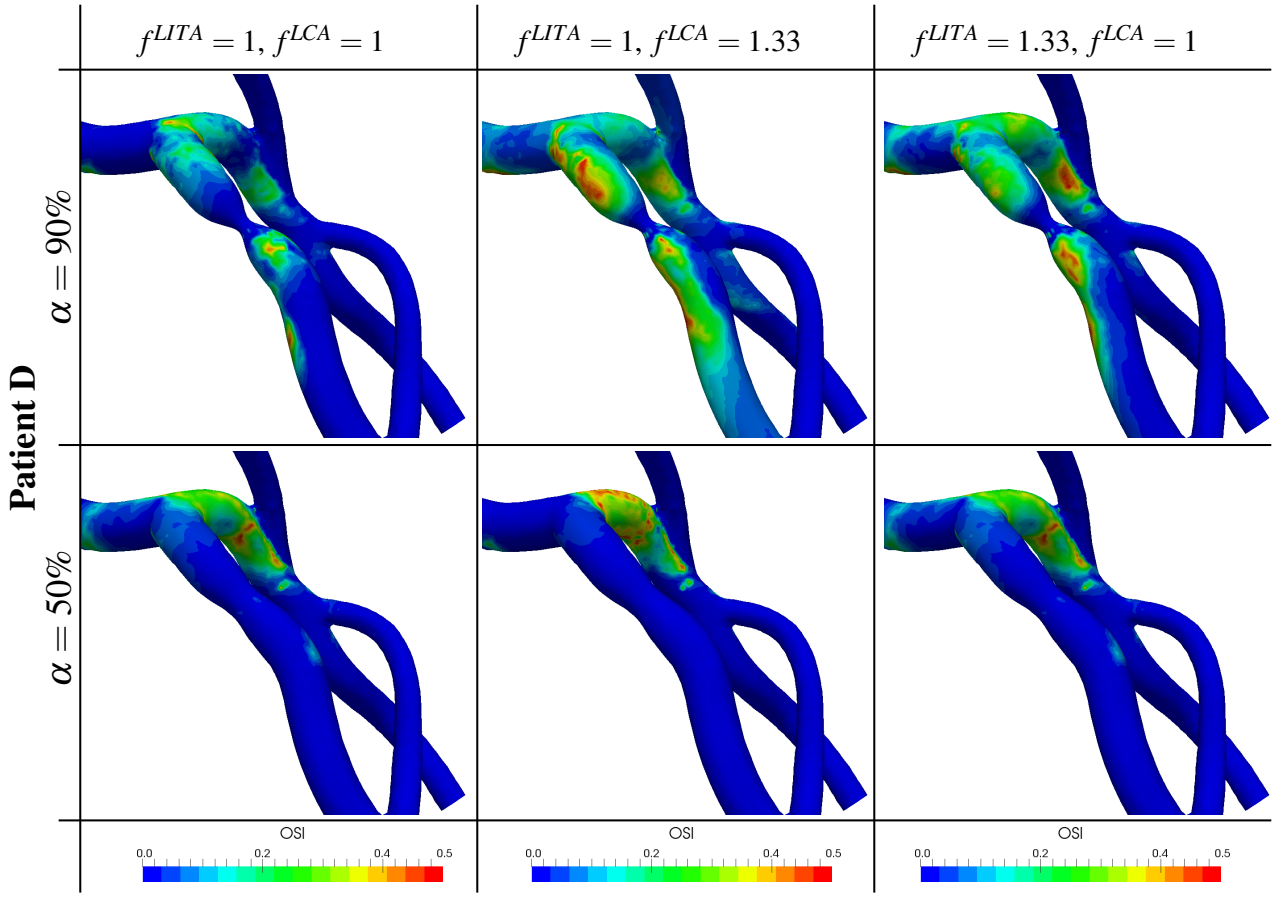

(b) OSI

Fig. 11: *Virtual scenario III*, LITA to Diag anastomosis, in a sequential graft: comparison of OSI for different inflow boundary conditions and stenosis.

plied to the three-dimensional patient-specific configuration in a post-processing stage. Moreover, the variation of grafting angles proposed in (Sankaran et al., 2012) requires a new segmentation for each new angle, as well as the variation of stenosis in (Guerciotti et al., 2016) requires a remeshing. Both are time consuming procedures that do not take advantage of the parametrized formulation. Instead, in this work we propose an automatic geometrical variation capable of exploiting the parametrization of the problem.

Overall, the most significant contribution of the proposed virtual surgery platform is to combine all these aspects into a *reduced order modelling framework*, capable of automatically handling physical and geometrical parameters, to numerically obtain quantities of interest in (as we will detail in the next section) a very fast way, reducing days of CPU time on a cluster to few minutes on a laptop. This is possible thanks to a specialized shape parametrization map, tailored for CABG networks, and projection-based ROM based on a

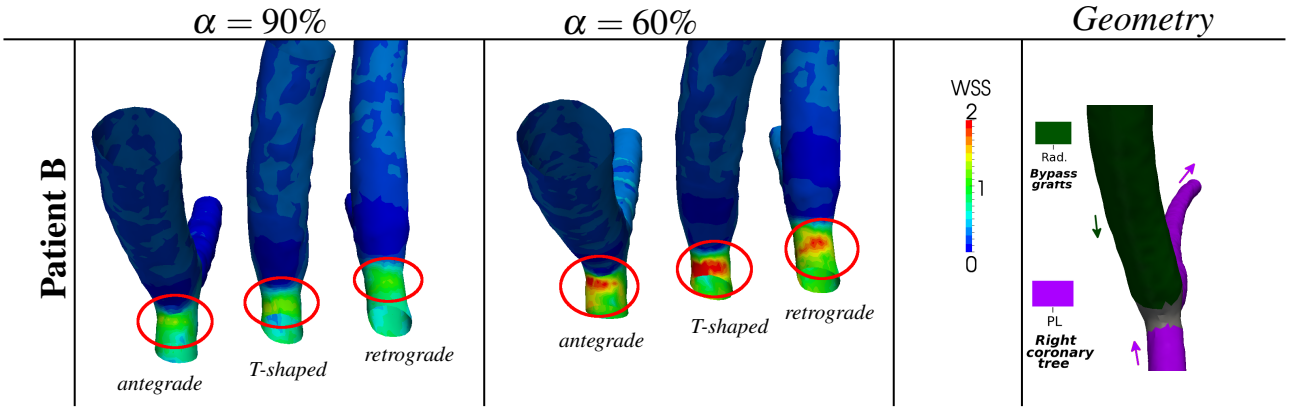

Fig. 12: *Virtual scenario III*, radial to PL anastomosis: comparison of WSS [Pa] for three anastomoses types.

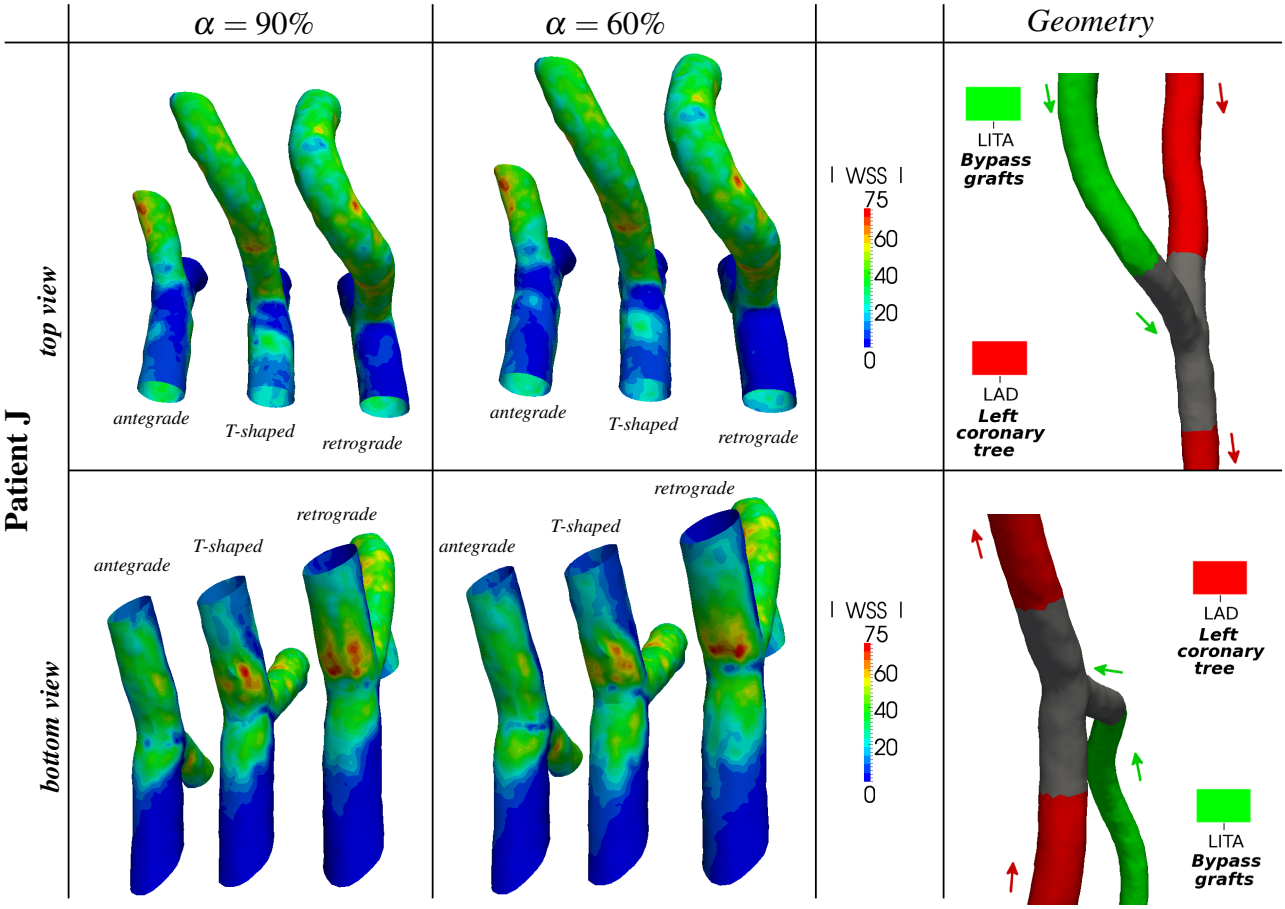

Fig. 13: *Virtual scenario IV*, *LITA to LAD anastomosis*: comparison of WSS [Pa] at peak systole for three anastomoses types.

POD–Galerkin approach for unsteady Navier-Stokes equations.

4.2 Computational performance of the virtual surgery platform

Details of the virtual surgery platform are provided in Table 2. The high fidelity discretization is queried only during the offline stage (see Section 2.3); instead, the online reduced model is used for each query to the virtual surgery

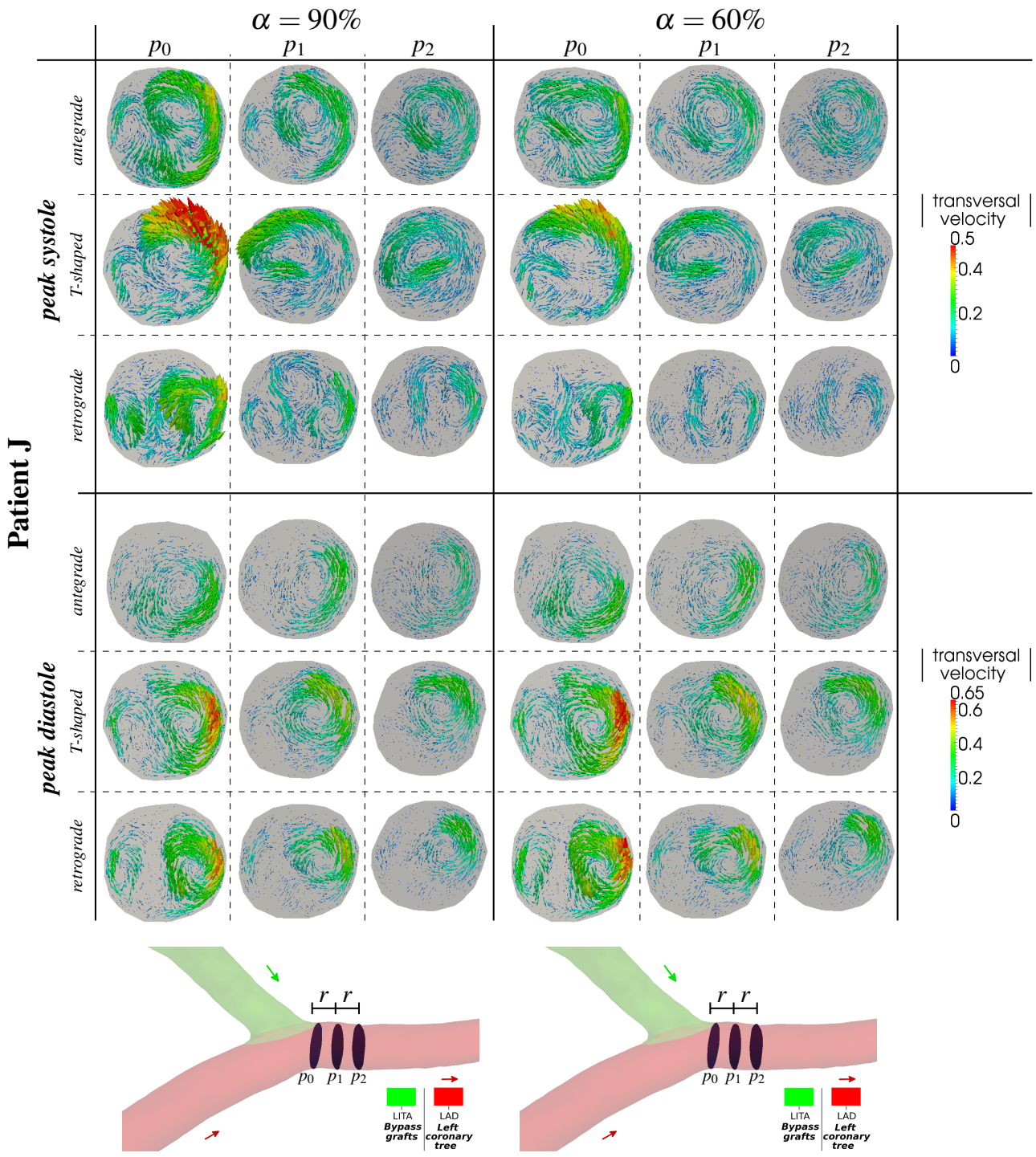

Fig. 14: *Virtual scenario IV*, LITA to LAD anastomosis: comparison of normalized transversal velocity profiles at different phases of the cardiac cycle for three anastomoses types.

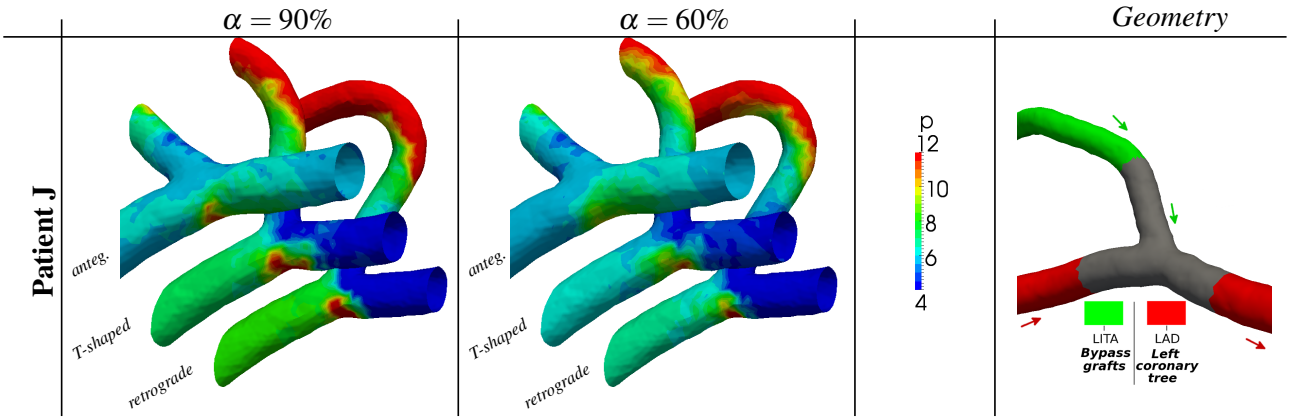

Fig. 15: *Virtual scenario IV*, LITA to LAD anastomosis: comparison of pressure drop [mmHg] at peak systole for three anastomoses types.

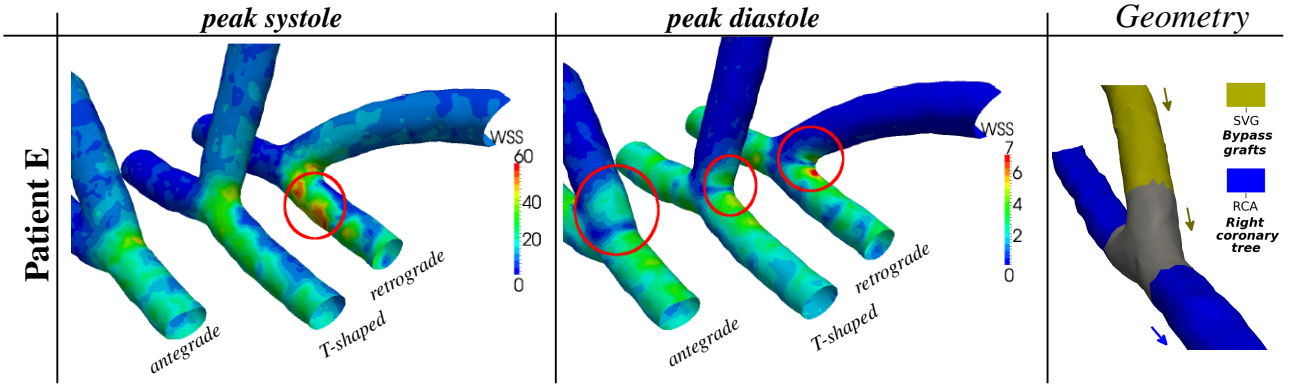

Fig. 16: *Virtual scenario IV*, SVG to PDA anastomosis: comparison of WSS [Pa] at different phases of the cardiac cycle for three anastomoses types.

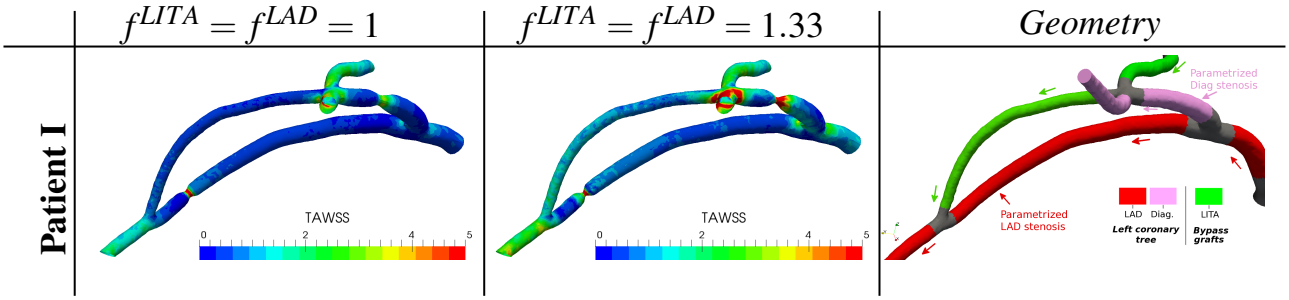

Fig. 17: *Virtual scenario V*, LITA-Diag-LAD sequential graft: comparison of TAWSS for different inflow boundary conditions and stenosis.

platform. The total number of degrees of freedom for the high fidelity simulation is of order 10^6, while a considerably smaller number of degrees of freedom, corresponding to 150 reduced basis functions (accounting for both velocity and pressure approximation) are required in the reduced order model. These reduced basis functions account for 99% of the information retained in the snapshots on Ξ_{train}, selected during the offline stage. As shown in Ballarin et al. (2016), these basis functions accurately approximate the solution with an error less than 1%, so that the evaluation of the reduced model can be used in place of the high fidelity one without any significant loss of accuracy.

The considerable reduction of degrees of freedom entails large computational savings in the proposed reduced order framework. In fact, high fidelity simulations are performed in parallel, on 32 processors, and require approxi-

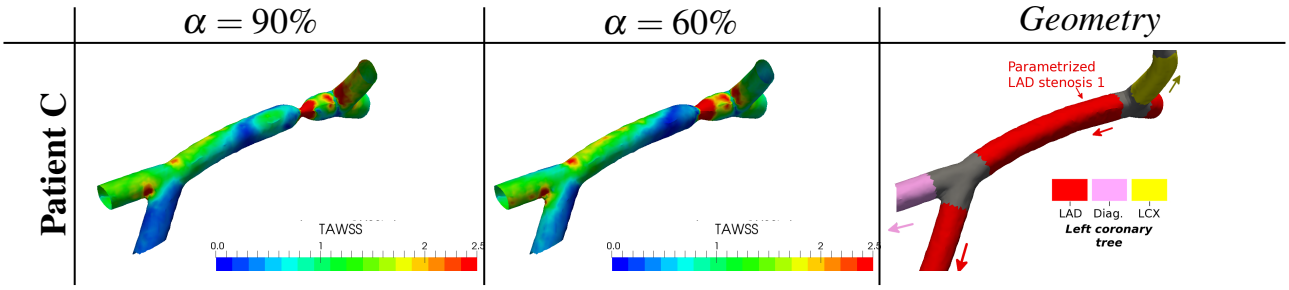

Fig. 18: *Virtual scenario V*, LAD-LCX and LAD-Diag bifurcations: comparison of TAWSS [Pa] for different inflow boundary conditions and stenosis.

mately 10 wall time hours per cardiac cycle (to be multiplied by the number of processors to obtain the actual CPU time, as listed in Table 2). Reduced order simulations, instead, are performed on a single processor and require only CPU times of the order of minutes, with computational savings in terms of user time up to 99%. Thus, the main advantage of the proposed reduced order approach is its capability to compare several different physical or geometrical configurations in computational times considerably smaller than ones obtained by standard finite element simulations, still preserving the same degree of accuracy.

4.3 Discussion of the results of the virtual surgery platform for each scenario

4.3.1 Virtual scenario I: effect of flow rate variation in Y-grafts

TAWSS results summarized in Figures 7 (Y-graft with arterial graft) and Figure 8 (Y-graft with venous graft) highlight the formation of a critical region, characterized by high TAWSS, on the LITA near the Y-graft. In all cases, a region of comparable TAWSS is present also in the radial artery (see, in particular, Patient A) and SVG (see, in particular, Patient F), although the surface extension of the region of high TAWSS is larger in the LITA than in the other graft (see, in particular, Patients F and G). The region of high TAWSS is highly sensitive to the graft flow (f^{LITA}), and features a larger area increasing graft flow in all cases. Local geometrical features also influence the behavior of TAWSS: high values appear in the LITA graft proximally to the Y-graft where the graft features high curvature (see in particular Patients F, H, I). Moreover, maximum values of TAWSS are higher when the bifurcation angle between the two grafts is increased (compare Patient A to C, and Patient I to H).

4.3.2 Virtual scenario II: effect of flow rate variation in sequential grafts

Results in Figure 9 highlight that, in all cases, a region of high TAWSS is found at the arterial beds of native coronary arteries, distal to the anastomosis. Moreover, in the case of cross anastomosis (Patient A), the region of maximum WSS near the OM (first cross anastomosis from the top) is slightly larger than the one near the LCX (second cross anastomosis from the top). A similar behavior can be noticed in the flow case, where the latero-lateral anastomosis features higher WSS on the arterial bed than the termino-lateral anastomosis in Patient G, as in Patient C, where the first anastomosis is the most critical, as it features the highest WSS values, which gradually decrease at the remaining anastomoses. The magnitude of WSS on the arterial bed at the latero-lateral anastomosis is more sensible to increased graft flow rates in the flow direction case than the cross one. This is due to the fact that flow direction anastomosis of Patients C and G are supplied directly by LITA (where increased graft flow rate is enforced), while cross anastomosis by radial artery of Patient A is only partially affected by the increased flow rate, because of the proximal flow split in the Y-graft between radial and LITA arteries.

4.3.3 Virtual scenario III: effect of flow rate and stenosis variation on anastomosis

We first consider anastomoses on the left coronary tree. Figure 10 shows the OSI near the anastomosis for different values of proximal stenosis (90%, 80%, 60%, 0%) near a LITA-LAD end-to-side anastomosis. It is well agreed in the clinical community that LITA is the gold standard for surgeries on the LAD, and that employing a LITA bypass graft on a non-critical stenosis may lead to early graft occlusion (Hillis et al., 2011). The study on Patient B provides a numerical confirmation of the dependence of fluid dynamics indices on stenosis factors. OSI assumes its maximum values near the toe of the graft, and the size of the area of maximum OSI increases for decreasing proximal stenosis. This can be

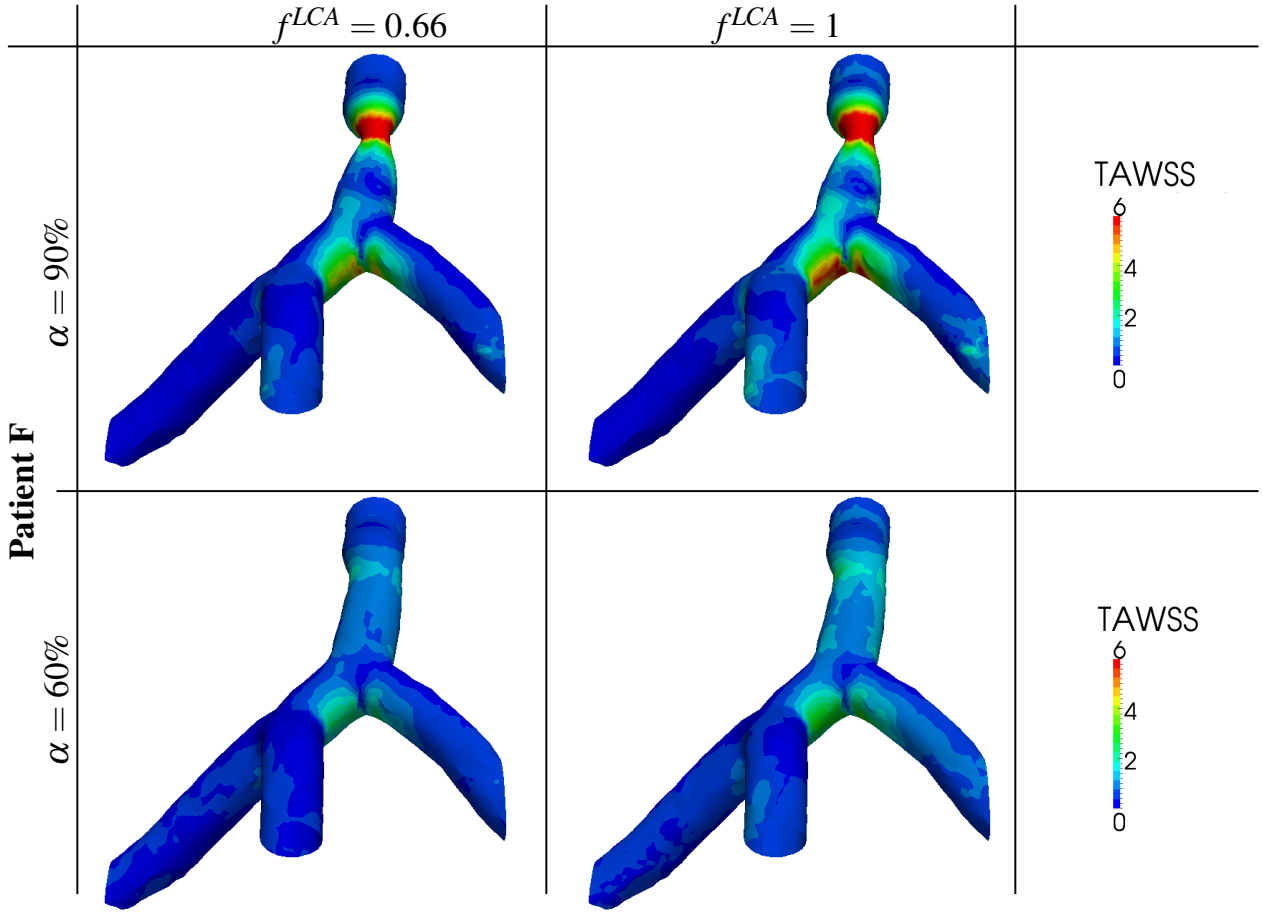

(a)

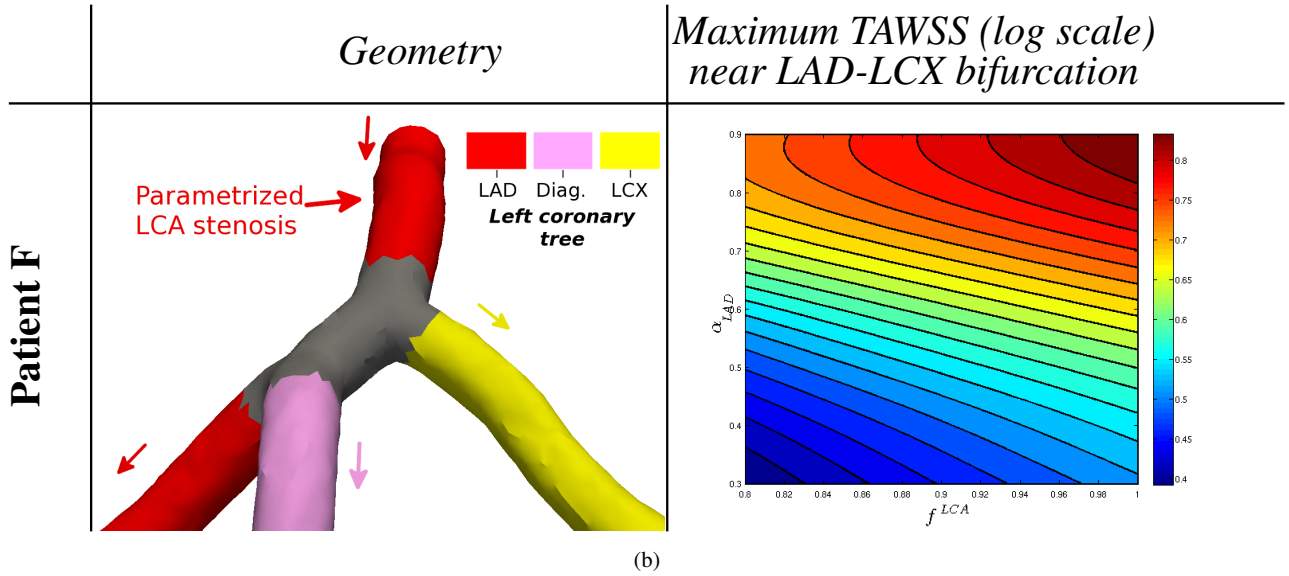

(b)

Fig. 19: *Virtual scenario V*, LAD-LCX bifurcation: comparison of TAWSS [Pa] for different inflow boundary conditions and stenosis.

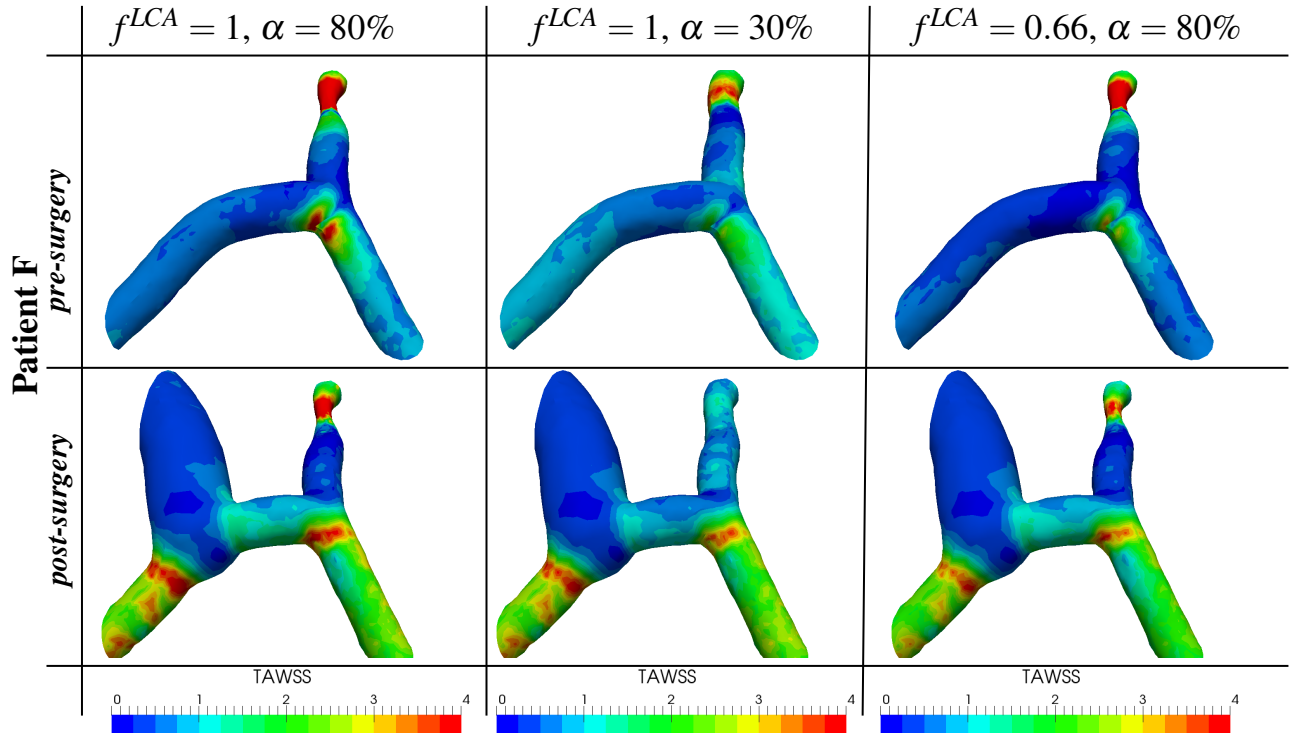

(a)

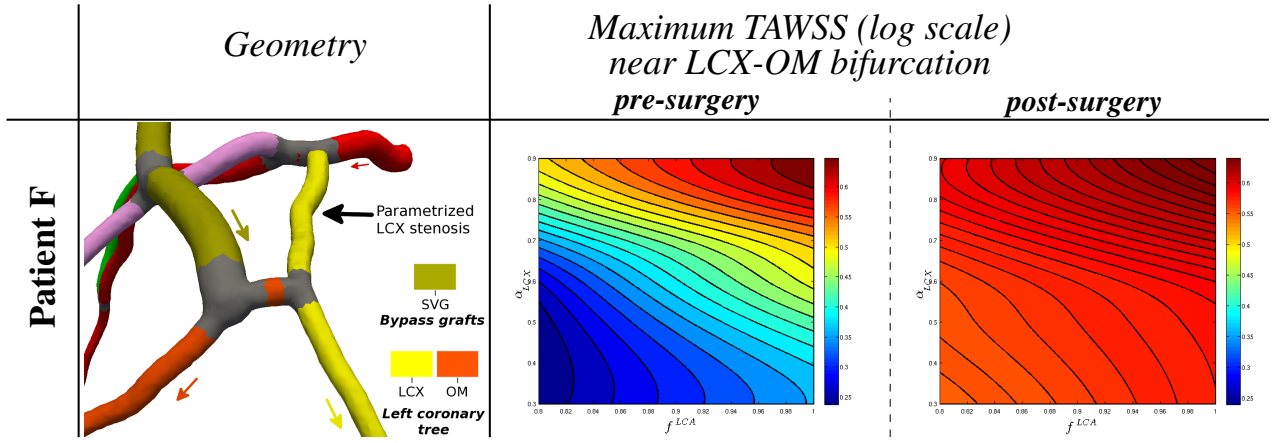

(b)

Fig. 20: *Virtual scenario V*, LCX-OM bifurcation: comparison of TAWSS [Pa], both pre- and post-surgery, for different inflow boundary conditions and stenosis.

motivated by the higher residual flow in the LAD. This result is in agreement with the current clinical practice (Hillis et al., 2011). Moreover, OSI assumes its maximum value in the LAD, proximal to the anastomosis, for all values of proximal stenosis.

Similar results are obtained for a more complete parametrization (on both flow rates and stenosis factors) on a more complex surgery (sequential LITA-Diag-LAD). Results in Figure 11 show that parametrized flow rates do not have significant effects on the OSI for non critical stenosis (second row). Instead, for more severe stenosis (first row), possible critical regions of the surgery, as highlighted by large values of OSI, are located near the LITA-Diag anastomosis (especially for increased graft flow rates, first row, right) and proximally and distally to the stenosis (especially in the case of increased coronary flow rates, first row, middle).

Finally, we also consider the case of an arterial anastomosis on the right coronary network. Numerical results in Figure 12 show that maximum WSS values, located near the heel of the graft, increases as the stenosis decreases: this is in agreement with the current clinical practice, that prescribes the usage of radial artery as a graft only when stenosis is

greater than 70% (Desai et al., 2004; Moran et al., 2001; Yie et al., 2008; Nicolini et al., 2014). This behavior does not depend strongly on the considered anastomosis (antegrade, T-shaped, retrograde).

4.3.4 Case IV: anastomosis variation

As in the previous section, we first compare different terminolateral LITA-LAD anastomosis (left coronary network), corresponding to antegrade, T-shaped and retrograde anastomoses. Current clinical experience and anatomical considerations suggest the use of antegrade anastomosis (Kirklin and Barratt-Boyes, 1988). The results summarized in Figures 13-15 provide numerical evidence of this approach. Figure 13 shows a comparison of WSS distribution for the three anastomoses types and two different values of stenosis severity (critical: 90% and non-critical 60%). The results are provided for $t = 0.15\ s$ (peak LITA flow in systolic phase), since at this phase of the cardiac cycle the differences are more clearly visible. Both T-shaped and retrograde anastomoses feature worse patterns than the antegrade one since:

(i) at the distal arterial floor, maximum WSS values in T-shaped and retrograde cases are approximately two times higher than in the antegrade case. This pattern remains unchanged for different stenosis severities;
(ii) intermediate WSS values are also observed in the proximal part of the arterial floor. This region is larger for T-shaped and retrograde anastomoses than the antegrade, although minimum and maximum value are not affected by the anastomosis type. Moreover, this region enlarges as the degree of proximal stenosis decreases, because of the higher residual flow in the native coronary;
(iii) in all anastomoses, the region downstream to the toe features low WSS.

The analysis of transversal velocity profiles (normalized by the maximum velocity in the anastomosis, at the same time) is carried out in Figure 14, at $t = 0.15\ s$ (peak LITA flow in systolic phase) and $t = 0.55\ s$ (peak LCA flow in diastolic phase). In all anastomoses, Dean vortices appear in the region of the anastomosis. Peak values of transversal velocity are reached at $t = 0.55\ s$. In agreement with the previous discussion, both T-shaped and retrograde anastomoses feature worse patterns than the antegrade one since:

(i) Dean vortices are dissipated more quickly in the antegrade anastomosis than in T-shaped and retrograde ones;
(ii) antegrade anastomosis features lower transversal than both T-shaped and retrograde anastomoses in the section closest to the anastomosis. At $t = 0.15\ s$ T-shaped anastomosis features the highest transversal velocity, while a similar behavior among T-shaped and retrograde cases is observed for $t = 0.55\ s$;
(iii) a third vortex may be formed in retrograde anastomosis, especially for high stenosis and a peak LITA flow. This is particularly apparent in the second slice on the third row of Figure 14(a).

Moreover, Figure 15 shows a comparison of the pressure drop in the three different anastomoses. The pressure drop is minimum for antegrade anastomosis; T-shaped and retrograde anastomoses feature instead an higher pressure drop. Moreover, an higher pressure drop across the anastomosis is obtained decreasing the stenosis severity; this is an additional confirmation of the clinical experience that a CABG surgery should be performed only for critical stenoses.

A different behavior can be observed instead when considering a venous, rather than a LITA graft, on the right coronary tree. Vein grafts are usually characterized by a larger radius. In particular, Figure 16 reports a comparison of WSS at different phases of the cardiac cycle for three anastomoses types, highlighting that T-shaped anastomosis feature comparable patterns to antegrade anastomosis. Also in this case, the result is in good agreement with current clinical practice, which prescribes the use of T-shaped grafts due to anatomical considerations (Kirklin and Barratt-Boyes, 1988). Our numerical results show that, in the retrograde case, maximum values of WSS are observed on the lateral arterial surface distal to the anastomosis and near the toe of the graft. The WSS magnitude in these regions is almost twice the magnitude in the antegrade and T-shaped cases.

4.3.5 Virtual scenario V: effect of flow rate and stenosis variation on native coronary bifurcations

Since the aim of this work is mainly related to the study of bypass grafts, in the previous sections we focused our attention only on anastomoses. However, similar studies can be carried out on native coronary bifurcations as well, which are also possible critical regions (before and) after the surgery. Thanks to capability to perform parametrized evaluations through the reduced order model it is possible to consider several different coronary artery flow rates, corresponding to either standard ($f^{LCA} = 1$), increased ($f^{LCA} = 1.33$) or decreased ($f^{LCA} = 0.8$) flow rates, or different stenosis severity, either critical ($\alpha_{LAD} = 80\%$) or non-critical ($\alpha_{LAD} = 30\%$). Critical regions, characterized by high WSS, are present at the bifurcations in all considered cases (LAD-Diag bifurcation for Patient I in Figure 17, LAD-LCX and LAD-Diag for Patient C in Figure 18, and LAD-LCX for Patient F in Figure 19). For instance, the effect of increased LCA flow rates is visible for Patient I at the LAD-Diag bifurcation; this is related to the presence of locally higher WSS at the LAD wall both proximally and distally the bifurcation. The arterial wall near the bifurcation features high WSS also in Patient F (Figure 19); maximum WSS values are influenced both by the inlet flow rate at the LCA ostium and the severity

of the LCA stenosis. In fact, lower values of the former parameter cause a smaller region of high WSS (compare Figure 19(a) by row). Moreover, the impingement of the jet of high velocity, caused by critical stenosis, on the arterial wall, is an additional cause of higher WSS (compare Figure 19(a) by column). Finally, we provide a plot of the maximum WSS for a wide range of stenosis severity and inlet flow rates in Figure 19(b); being able to query almost inexpensively our reduced order framework is the cornerstone in order to perform the analysis yielding this plot, that would have otherwise required several weeks of computational times if relying on traditional high-fidelity techniques.

A similar study can also be performed both before and after the surgery. In particular, we summarize in Figure 20 the results for the LCX-OM bifurcation of Patient F, which, in the post-surgical stage, is also perfused and affected by the blood flow from a saphenous vein graft. The results in Figure 20(a) compare the WSS near the bifurcation for critical stenosis ($\alpha_{LAD} = 80\%$) and standard native coronary flow ($f^{LCA} = 1$), non-critical stenosis ($\alpha_{LAD} = 30\%$) and standard ($f^{LCA} = 1$) native coronary flow, critical stenosis and decreased ($f^{LCA} = 0.8$) native coronary flow. The pattern of WSS at the bifurcation before the surgery, summarized in Figure 20(b), is similar to the one at the LAD-LCX bifurcation of the same Patient (discussed in the previous section), although smaller values of WSS are identified. On the other hand, after the surgery maximum values of WSS (Figure (c)) are less sensible to LCA inlet flow rate and stenosis factors. This is motivated by the fact that, in this case, the SVG graft is the main source of blood flow for both LCX and OM branches.

5 Conclusions

In this work we have taken advantage of a reduced order computational framework first proposed in proposed in (Ballarin et al., 2016) for the study of the haemodynamics in several patient-specific coronary artery bypass grafts (CABGs). The main aim of this work is to handle in a fast and efficient way simulations on *(i)* patient specific geometries, *(ii)* characterized by different parameters, and *(iii)* employing reduced order models to cut down large computational costs. The clinical dataset we employed features a large variability on diseased coronary arteries and bypass grafts. For the sake of comparison between different scenarios (related to either blood flow rates, disease or surgery choices) on the same patient-specific configuration, a parametrized formulation has been introduced. Several numerical results and parametric analyses have been provided. In particular,

I. the comparison of different Y-graft has highlighted different behaviors for radial and saphenous vein grafts (lower WSS on the former), and the presence of critical regions especially near the Y-graft for increased flow rates;
II. in a similar way, critical regions near the arterial bed are detected in case of sequential anastomoses;
III. surgery outcomes for different stenosis in native coronary arteries have been studied; the obtained results are in good agreement with clinical practice, that prescribes to undergo surgery only for critical stenoses. In particular, we have analyzed a LITA-LAD anastomosis, showing that a larger region of high oscillatory shear index appears near the toe of the graft if the stenosis is not critical, and a radial-PL anastomosis, showing that increased wall shear stress is present near the heel of the graft for non critical stenosis;
IV. variation of anastomosis, either of LITA-LAD or SVG-PDA anastomoses, has been discussed. The results of our virtual surgery framework are in agreement with current clinical practice, that suggests the use of antegrade anastomoses in LITA-LAD and the use of T-shaped anastomoses on the right coronary tree. These conclusions have been obtained performing comparison of WSS, transversal velocity profiles and pressure drop for three different anastomosis configurations, representative of antegrade, T-shaped and retrograde-flow anastomoses;
V. finally, the proposed framework has been exploited for evaluating flow patterns at native coronary artery bifurcations, also performing a comparison before and after surgery.

The proposed virtual surgery platform exploits a model reduction framework, capable of automatically handling physical and geometrical parameters, to numerically obtain quantities of interest in a very fast way (order of few minutes on a laptop). This can represent an attractive platform for the rapid study of complex CABG networks that frequently occur in the clinical practice.

Acknowledgments

Francesco Ballarin and Elena Faggiano acknowledge the support of the PRIN project “Mathematical and numerical modelling of the cardiovascular system, and their clinical applications”. Gianluigi Rozza acknowledges the SISSA Excellence Grant NOFYSAS “Computational and Geometrical Reduction Strategies for the simulation, control and optimization of complex systems”. We also acknowledge ERC Advanced Grant Mathcard (number 227058). We acknowledge the use of CINECA supercomputing facilities within the projects “Convenzione di Ateneo” agreement between Politecnico di Milano and CINECA, and “COGESTRA” between SISSA and CINECA, and Istituto Nazionale di Fisica Nucleare, within the project SUMA. We acknowledge the use of a customized version of the library `rbOOmit` within

`libMesh` (Knezevic and Peterson, 2011; Kirk et al., 2006) for the numerical simulations, and of the Vascular Modelling Toolkit `vmtk` (Antiga et al., 2008) and `3DSlicer` (Fedorov et al., 2012) for the medical imaging pipeline.

References

Antiga, L. (2002). *Patient-Specific Modeling of Geometry and Blood Flow in Large Arteries*. PhD thesis, Dipartimento di Bioingegneria, Politecnico di Milano.

Antiga, L., Ene-Iordache, B., and Remuzzi, A. (2003). Computational geometry for patient-specific reconstruction and meshing of blood vessels from MR and CT angiography. *IEEE Transactions on Medical Imaging*, 22(5):674–684.

Antiga, L., Piccinelli, M., Botti, L., Ene-Iordache, B., Remuzzi, A., and Steinman, D. (2008). An image-based modeling framework for patient-specific computational hemodynamics. *Medical and Biological Engineering and Computing*, 46:1097–1112.

Ballarin, F. (2015). *Reduced-order models for patient-specific haemodynamics of coronary artery bypass grafts*. PhD thesis, Department of Mathematics, Politecnico di Milano. `http://hdl.handle.net/10589/102804`.

Ballarin, F., Faggiano, E., Ippolito, S., Manzoni, A., Quarteroni, A., Rozza, G., and Scrofani, R. (2016). Fast simulations of patient-specific haemodynamics of coronary artery bypass grafts based on a POD–Galerkin method and a vascular shape parametrization. *Journal of Computational Physics*, 315:609–628.

Ballarin, F., Manzoni, A., Quarteroni, A., and Rozza, G. (2015). Supremizer stabilization of POD–Galerkin approximation of parametrized steady incompressible Navier–Stokes equations. *International Journal for Numerical Methods in Engineering*, 102(5):1136–1161.

Berkooz, G., Holmes, P., and Lumley, J. (1993). The Proper Orthogonal Decomposition in the Analysis of Turbulent Flows. *Annu. Rev. Fluid Mech.*, 25(1):539–575.

Bertolotti, C. and Deplano, V. (2000). Three-dimensional numerical simulations of flow through a stenosed coronary bypass. *Journal of Biomechanics*, 33(8):1011–1022.

Bertolotti, C., Deplano, V., Fuseri, J., and Dupouy, P. J. (2001). Numerical and experimental models of post-operative realistic flows in stenosed coronary bypasses. *Journal of Biomechanics*, 34(8):1049–1064.

Bishop, R. L. (1975). There is more than one way to frame a curve. *American Mathematical Monthly*, 82(3):246–251.

Bonert, M., Myers, J. G., Fremes, S., Williams, J., and Ross Ethier, C. (2002). A numerical study of blood flow in coronary artery bypass graft side-to-side anastomoses. *Annals of Biomedical Engineering*, 30(5):599–611.

Boutsianis, E., Dave, H., Frauenfelder, T., Poulikakos, D., Wildermuth, S., Turina, M., Ventikos, Y., and Zund, G. (2004). Computational simulation of intracoronary flow based on real coronary geometry. *European Journal of Cardio-Thoracic Surgery*, 26(2):248–256.

Burkardt, J., Gunzburger, M., and Lee, H.-C. (2006). POD and CVT-based reduced-order modeling of Navier–Stokes flows. *Computer Methods in Applied Mechanics and Engineering*, 196(1–3):337–355.

Chaichana, T., Sun, Z., and Jewkes, J. (2011). Computation of hemodynamics in the left coronary artery with variable angulations. *Journal of biomechanics*, 44(10):1869–1878.

Deplano, V., Bertolotti, C., and Boiron, O. (2001). Numerical simulations of unsteady flows in a stenosed coronary bypass graft. *Medical and Biological Engineering and Computing*, 39(4):488–499.

Desai, N. D., Cohen, E. A., Naylor, C. D., and Fremes, S. E. (2004). A randomized comparison of radial-artery and saphenous-vein coronary bypass grafts. *New England Journal of Medicine*, 351(22):2302–2309.

Do, H., Owida, A. A., Yang, W., and Morsi, Y. S. (2011). Numerical simulation of the haemodynamics in end-to-side anastomoses. *International Journal for Numerical Methods in Fluids*, 67:638–650.

Dur, O., Coskun, S., Coskun, K., Frakes, D., Kara, L., and Pekkan, K. (2011). Computer-aided patient-specific coronary artery graft design improvements using CFD coupled shape optimizer. *Cardiovascular Engineering and Technology*, 2:35–47.

Fedorov, A., Beichel, R., Kalpathy-Cramer, J., Finet, J., Fillion-Robin, J.-C., Pujol, S., Bauer, C., Jennings, D., Fennessy, F., Sonka, M., Buatti, J., Aylward, S., Miller, J. V., Pieper, S., and Kikinis, R. (2012). 3D Slicer as an image computing platform for the quantitative imaging network. *Magnetic Resonance Imaging*, 30(9):1323–1341.

Fei, D.-Y., Thomas, J. D., and Rittgers, S. E. (1994). The effect of angle and flow rate upon hemodynamics in distal vascular graft anastomoses: a numerical model study. *Journal of Biomechanical Engineering*, 116(3):331–336.

Frangi, A. F., Niessen, W. J., Vincken, K. L., and Viergever, M. A. (1998). Multiscale vessel enhancement filtering. In Wells, W. M., Colchester, A., and Delp, S., editors, *Medical Image Computing and Computer-Assisted Intervention — MICCAI'98*, volume 1496 of *Lecture Notes in Computer Science*, pages 130–137. Springer Berlin Heidelberg.

Frauenfelder, T., Boutsianis, E., Schertler, T., Husmann, L., Leschka, S., Poulikakos, D., Marincek, B., and Alkadhi, H. (2007). Flow and wall shear stress in end-to-side and side-to-side anastomosis of venous coronary artery bypass grafts. *BioMedical Engineering OnLine*, 6(1):35:1–35:13.

Freshwater, I. J., Morsi, Y. S., and Lai, T. (2006). The effect of angle on wall shear stresses in a LIMA to LAD anastomosis: numerical modelling of pulsatile flow. *Proceedings of the Institution of Mechanical Engineers, Part H: Journal of Engineering in Medicine*, 220(7):743–757.

Ghista, D. and Kabinejadian, F. (2013). Coronary artery bypass grafting hemodynamics and anastomosis design: a biomedical engineering review. *BioMedical Engineering OnLine*, 12(1):129:1–129:28.

Giordana, S., Sherwin, S., Peiró, J., Doorly, D., Crane, J., Lee, K., Cheshire, N., and Caro, C. (2005). Local and global geometric influence on steady flow in distal anastomoses of peripheral bypass grafts. *J. Biomech. Engr.*, 127:1087.

Go, A. S., Mozaffarian, D., Roger, V. L., Benjamin, E. J., Berry, J. D., Blaha, M. J., Dai, S., Ford, E. S., et al. (2014). Executive summary: Heart disease and stroke statistics–2014 update: a report from the American Heart Association. *Circulation*, 129(3):399–410.

Guerciotti, B., Vergara, C., Ippolito, S., Quarteroni, A., Antona, C., and Scrofani, R. (2016). Computational study of the risk of restenosis in coronary bypasses. *Biomechanics and Modeling in Mechanobiology*.

Hesthaven, J. S., Rozza, G., and Stamm, B. (2016). *Certified Reduced Basis Methods for Parametrized Partial Differential Equations*. SpringerBriefs in Mathematics. Springer International Publishing.

Hillis, L. D., Smith, P. K., et al. (2011). 2011 ACCF/AHA guideline for coronary artery bypass graft surgery – a report of the American College of Cardiology Foundation/American Heart Association task force on practice guidelines developed in collaboration with the american association for thoracic surgery, society of cardiovascular anesthesiologists, and society of thoracic surgeons. *Journal of the American College of Cardiology*, 58(24):e123–e210.

Idu, M. M., Buth, J., Hop, W. C. J., Cuypers, P., van de Pavoordt, E. D. W. M., and Tordoir, J. M. H. (1999). Factors influencing the development of vein-graft stenosis and their significance for clinical management. *European Journal of Vascular and Endovascular Surgery*, 17(1):15–21.

Inzoli, F., Migliavacca, F., and Pennati, G. (1996). Numerical analysis of steady flow in aorto-coronary bypass 3-D model. *Journal of Biomechanical Engineering*, 118(2):172–179.

Ishida, N., Sakuma, H., Cruz, B. P., Shimono, T., Tokui, T., Yada, I., Takeda, K., and Higgins, C. B. (2001). MR flow measurement in the internal mammary artery–to–coronary artery bypass graft: comparison with graft stenosis at radiographic angiography. *Radiology*, 220(2):441–447.

Jackson, Z. S., Ishibashi, H., Gotlieb, A. I., and Langille, B. L. (2001). Effects of anastomotic angle on vascular tissue responses at end-to-side arterial grafts. *Journal of Vascular Surgery*, 34(2):300–307.

Kabinejadian, F., Chua, L., Ghista, D., Sankaranarayanan, M., and Tan, Y. (2010). A novel coronary artery bypass graft design of sequential anastomoses. *Annals of Biomedical Engineering*, 38(10):3135–3150.

Kabinejadian, F. and Ghista, D. N. (2012). Compliant model of a coupled sequential coronary arterial bypass graft: effects of vessel wall elasticity and non-Newtonian rheology on blood flow regime and hemodynamic parameters distribution. *Medical Engineering & Physics*, 34(7):860–872.

Keegan, J., Gatehouse, P. D., Yang, G.-Z., and Firmin, D. N. (2004). Spiral phase velocity mapping of left and right coronary artery blood flow: correction for through-plane motion using selective fat-only excitation. *Journal of Magnetic Resonance Imaging*, 20(6):953–960.

Keynton, R. S., Shu, M. C. S., and Rittgers, S. E. (1991). The effect of angle and flow rate upon hemodynamics in distal vascular graft anastomoses: an in vitro model study. *Journal of Biomechanical Engineering*, 113(4):458–463.

Kim, H. J., Vignon-Clementel, I. E., Figueroa, C. A., Jansen, K. E., and Taylor, C. A. (2010). Developing computational methods for three-dimensional finite element simulations of coronary blood flow. *Finite Elements in Analysis and Design*, 46(6):514–525.

Kirk, B. S., Peterson, J. W., Stogner, R. H., and Carey, G. F. (2006). libMesh: a C++ library for parallel adaptive mesh refinement/coarsening simulations. *Engineering with Computers*, 22(3-4):237–254.

Kirklin, J. W. and Barratt-Boyes, B. G. (1988). *Cardiac surgery: morphology, diagnostic criteria, natural history, techniques, results, and indications*. Churchill Livingstone New York.

Kleinstreuer, C., Nazemi, M., and Archie, J. P. (1991). Hemodynamics analysis of a stenosed carotid bifurcation and its plaque-mitigating design. *Journal of Biomechanical Engineering*, 113(3):330–335.

Knezevic, D. J. and Peterson, J. W. (2011). A high-performance parallel implementation of the certified reduced basis method. *Computer Methods in Applied Mechanics and Engineering*, 200(13–16):1455–1466.

Ku, D. N., Giddens, D. P., Zarins, C. K., and Glagov, S. (1985). Pulsatile flow and atherosclerosis in the human carotid bifurcation. Positive correlation between plaque location and low oscillating shear stress. *Arteriosclerosis, Thrombosis, and Vascular Biology*, 5(3):293–302.

Kute, S. M. and Vorp, D. A. (2001). The effect of proximal artery flow on the hemodynamics at the distal anastomosis of a vascular bypass graft: computational study. *Journal of Biomechanical Engineering*, 123(3):277–283.

Lei, M., Archie, J. P., and Kleinstreuer, C. (1997). Computational design of a bypass graft that minimizes wall shear

stress gradients in the region of the distal anastomosis. *Journal of Vascular Surgery*, 25(4):637–646.

Lei, M., Giddens, D. P., Jones, S. A., Loth, F., and Bassiouny, H. (2000). Pulsatile flow in an end-to-side vascular graft model: comparison of computations with experimental data. *Journal of Biomechanical Engineering*, 123(1):80–87.

Lorensen, W. E. and Cline, H. E. (1987). Marching cubes: A high resolution 3d surface construction algorithm. *Computer Graphics*, 21(4):163–169.

Loth, F., Fischer, P. F., and Bassiouny, H. S. (2008). Blood flow in end-to-side anastomoses. *Annual Review of Fluid Mechanics*, 40:367–393.

Manzoni, A. (2014). An efficient computational framework for reduced basis approximation and a posteriori error estimation of parametrized Navier–Stokes flows. *ESAIM: Mathematical Modelling and Numerical Analysis*, 48:1199–1226.

Marsden, A. L. (2014). Optimization in cardiovascular modeling. *Annual Review of Fluid Mechanics*, 46(1):519–546.

Marsden, A. L., Feinstein, J. A., and Taylor, C. A. (2008). A computational framework for derivative-free optimization of cardiovascular geometries. *Computer Methods in Applied Mechanics and Engineering*, 197(21-24):1890–1905.

Migliavacca, F. and Dubini, G. (2005). Computational modeling of vascular anastomoses. *Biomechanics and Modeling in Mechanobiology*, 3(4):235–250.

Moran, S. V., Baeza, R., Guarda, E., Zalaquett, R., Irarrazaval, M. J., Marchant, E., and Deck, C. (2001). Predictors of radial artery patency for coronary bypass operations. *The Annals of Thoracic Surgery*, 72(5):1552–1556.

Nicolini, F., Agostinelli, A., Spaggiari, I., Vezzani, A., Benassi, F., Maestri, F., and Gherli, T. (2014). Current trends in surgical revascularization of multivessel coronary artery disease with arterial grafts. *International Heart Journal*, 55(5):381–385.

Nordgaard, H., Swillens, A., Nordhaug, D., Kirkeby-Garstad, I., Van Loo, D., Vitale, N., Segers, P., Haaverstad, R., and Lovstakken, L. (2010). Impact of competitive flow on wall shear stress in coronary surgery: computational fluid dynamics of a LIMA–LAD model. *Cardiovascular Research*, 88(3):512–519.

Owida, A. A., Do, H., and Morsi, Y. S. (2012). Numerical analysis of coronary artery bypass grafts: an over view. *Computer Methods and Programs in Biomedicine*, 108(2):689–705.

Pagni, S., Storey, J., Ballen, J., Montgomery, W., Qaqish, N. K., Etoch, S., and Spence, P. A. (1997). Factors affecting internal mammary artery graft survival: how is competitive flow from a patent native coronary vessel a risk factor? *Journal of Surgical Research*, 71(2):172–178.

Perona, P. and Malik, J. (1990). Scale-space and edge detection using anisotropic diffusion. *Pattern Analysis and Machine Intelligence, IEEE Transactions on*, 12(7):629–639.

Politis, A. K., Stavropoulos, G. P., Christolis, M. N., Panagopoulos, P. G., Vlachos, N. S., and Markatos, N. C. (2008). Numerical modelling of simulated blood flow in idealized composite arterial coronary grafts: transient flow. *Journal of Biomechanics*, 41(1):25–39.

Probst, M., Lülfesmann, M., Nicolai, M., Bücker, H. M., Behr, M., and Bischof, C. H. (2010). Sensitivity of optimal shapes of artificial grafts with respect to flow parameters. *Computer Methods in Applied Mechanics and Engineering*, 199(17-20):997–1005.

Puskas, J. D., Lazar, H. L., Mack, M. J., Sabik III, J. F., and Taggart, D. P. (2014). State-of-the-art coronary artery bypass graft. *Seminars in Thoracic and Cardiovascular Surgery*, 26(1):76–94.

Qiao, A. and Liu, Y. (2006). Influence of graft-host diameter ratio on the hemodynamics of CABG. *Bio-Medical Materials and Engineering*, 16(3):189–201.

Quarteroni, A., Manzoni, A., and Negri, F. (2016). *Reduced Basis Methods for Partial Differential Equations. An Introduction*, volume 92 of *Unitext*. Springer.

Ravindran, S. (2000). A reduced-order approach for optimal control of fluids using proper orthogonal decomposition. *Int. J. Numer. Meth. Fluids*, 34:425–448.

Ross Ethier, C., Steinman, D. A., Zhang, X., Karpik, S., and Ojha, M. (1998). Flow waveform effects on end-to-side anastomotic flow patterns. *Journal of Biomechanics*, 31(7):609–617.

Rowe, G. G., Thomsen, J. H., Stenlund, R. R., Mckenna, D. H., Sialer, S., and Corliss, R. J. (1969). A study of hemodynamics and coronary blood flow in man with coronary artery disease. *Circulation*, 39(1):139–148.

Rozza, G., Huynh, D. B. P., and Manzoni, A. (2013). Reduced basis approximation and a posteriori error estimation for Stokes flows in parametrized geometries: roles of the inf-sup stability constants. *Numerische Mathematik*, 125(1):115–152.

Sabik III, J. F. and Blackstone, E. H. (2008). Coronary artery bypass graft patency and competitive flow. *Journal of the American College of Cardiology*, 51(2):126–128.

Sabik III, J. F., Lytle, B. W., Blackstone, E. H., Houghtaling, P. L., and Cosgrove, D. M. (2005). Comparison of saphenous vein and internal thoracic artery graft patency by coronary system. *The Annals of Thoracic Surgery*, 79(2):544–551.

Sabik III, J. F., Lytle, B. W., Blackstone, E. H., Khan, M., Houghtaling, P. L., and Cosgrove, D. M. (2003). Does competitive flow reduce internal thoracic artery graft patency? *The Annals of Thoracic Surgery*, 76(5):1490–1497.

Sankaran, S., Esmaily Moghadam, M., Kahn, A., Tseng, E., Guccione, J., and Marsden, A. (2012). Patient-specific multiscale modeling of blood flow for coronary artery bypass graft surgery. *Annals of Biomedical Engineering*, 40:2228–2242.

Sankaran, S. and Marsden, A. L. (2010). The impact of uncertainty on shape optimization of idealized bypass graft models in unsteady flow. *Physics of Fluids*, 22(12):1–16.

Sherwin, S. J. and Doorly, D. J. (2003). Flow dynamics within model distal arterial bypass grafts. *Advances in Fluid Mechanics*, 34:327–374.

Sherwin, S. J., Shah, O., Doorly, D. J., Peiro, J., Papaharilaou, Y., Watkins, N., Caro, C. G., and Dumoulin, C. L. (1999). The influence of out-of-plane geometry on the flow within a distal end-to-side anastomosis. *Journal of Biomechanical Engineering*, 122(1):86–95.

Staalsen, N.-H., Ulrich, M., Winther, J., Pedersen, E. M., How, T., and Nygaard, H. (1995). The anastomosis angle does change the flow fields at vascular end-to-side anastomoses in vivo. *Journal of Vascular Surgery*, 21(3):460–471.

Swillens, A., De Witte, M., Nordgaard, H., Løvstakken, L., Van Loo, D., Trachet, B., Vierendeels, J., and Segers, P. (2012). Effect of the degree of LAD stenosis on "competitive flow" and flow field characteristics in LIMA-to-LAD bypass surgery. *Medical & Biological Engineering & Computing*, 50(8):839–849.

Taylor, C. A. and Draney, M. T. (2004). Experimental and computational methods in cardiovascular fluid mechanics. *Annual Review of Fluid Mechanics*, 36:197–231.

Towne, J. B., Schmitt, D. D., Seabrook, G. R., and Bandyk, D. F. (1991). The effect of vein diameter on patency of in situ grafts. *The Journal of cardiovascular surgery*, 32(2):192–196.

Wen, J., Zheng, T., Jiang, W., Deng, X., and Fan, Y. (2011). A comparative study of helical-type and traditional-type artery bypass grafts: numerical simulation. *American Society of Artificial Internal Organs Journal*, 57(5):399–406.

Xiong, F. L. and Chong, C. K. (2008). A parametric numerical investigation on haemodynamics in distal coronary anastomoses. *Medical Engineering & Physics*, 30(3):311–320.

Yie, K., Na, C.-Y., Oh, S. S., Kim, J.-H., Shinn, S.-H., and Seo, H.-J. (2008). Angiographic results of the radial artery graft patency according to the degree of native coronary stenosis. *European Journal of Cardio-Thoracic Surgery*, 33(3):341–348.

Recent publications:

MATHEMATICS INSTITUTE OF COMPUTATIONAL SCIENCE AND ENGINEERING
Section of Mathematics

Ecole Polytechnique Fédérale (EPFL)

CH-1015 Lausanne

25.2016 MICHELE PISARONI, FABIO NOBILE, PÉNÉLOPE LEYLAND:
A continuation multi level Monte Carlo (C-MLMC) method for uncertainty quantification in compressible aerodynamics

26.2016 ASSYR ABDULLE, ONDREJ BUDÁČ:
Multiscale model reduction methods for flow in heterogeneous porous media

27.2016 ASSYR ABDULLE, PATRICK HENNING:
Multiscale methods for wave problems in heterogeneous media

28.2016 ASSYR ABDULLE, ORANE JECKER:
On heterogeneous coupling of multiscale methods for problems with and without scale separation

29.2016 WOLFGANG HACKBUSCH, DANIEL KRESSNER, ANDRÉ USCHMAJEW:
Perturbation of higher-order singular values

30.2016 ASSYR ABDULLE, ONDREJ BUDÁČ, ANTOINE IMBODEN:
Multiscale methods and model order reduction for flow problems in three-scale porous media

31.2016 DANIEL KRESSNER, ANA ŠUŠNJARA:
Fast computation of spectral projectors of banded matrices

32.2016 NICCOLO DAL SANTO, SIMONE DEPARIS, ANDREA MANZONI, ALFIO QUARTERONI:
Multi space reduced basis preconditioners for large-scale parametrized PDEs

33.2016 ASSYR ABDULLE, MARTIN HUBER, SIMON LEMAIRE:
An optimization-based numerical method for diffusion problems with sign-changing coefficients

34.2016 ASSYR ABDULLE, ANDREA DI BLASIO:
Numerical homogenization and model order reduction for multiscale inverse problems

35.2016 PETAR SIRKOVIĆ:
A reduced basis approach to large-scale pseudospectra computation

36.2016 ASSYR ABDULLE, GRIGORIOS A. PAVLIOTIS, URBAIN VAES:
Spectral methods for multiscale stochastic differential equations

37.2016 NICOLAS GILLIS, ROBERT LUCE:
A fast gradient method for nonnegative sparse regression with self dictionary

38.2016 FRANCESCO BALLARIN, ELENA FAGGIANO, ANDREA MANZONI, GIANLUIGI ROZZA, ALFIO QUARTERONI, SONIA IPPOLITO, CARLO ANTONA, ROBERTO SCROFANI:
A fast virtual surgery platform for many scenarios haemodynamics of patient-specific coronary artery bypass grafts